



## Engineering of Electromechanical Oxides by Symmetry Breaking

Zhang, Haiwu; Vasiljevic, Milica; Bergne, Achilles; Park, Dae-Sung; Insinga, Andrea R.; Yun, Shinhee; Esposito, Vincenzo; Pryds, Nini

*Published in:*  
Advanced Materials Interfaces

*Link to article, DOI:*  
[10.1002/admi.202300083](https://doi.org/10.1002/admi.202300083)

*Publication date:*  
2023

*Document Version*  
Publisher's PDF, also known as Version of record

[Link back to DTU Orbit](#)

*Citation (APA):*  
Zhang, H., Vasiljevic, M., Bergne, A., Park, DS., Insinga, A. R., Yun, S., Esposito, V., & Pryds, N. (2023). Engineering of Electromechanical Oxides by Symmetry Breaking. *Advanced Materials Interfaces*, 10(18), Article 2300083. <https://doi.org/10.1002/admi.202300083>

---

### General rights

Copyright and moral rights for the publications made accessible in the public portal are retained by the authors and/or other copyright owners and it is a condition of accessing publications that users recognise and abide by the legal requirements associated with these rights.

- Users may download and print one copy of any publication from the public portal for the purpose of private study or research.
- You may not further distribute the material or use it for any profit-making activity or commercial gain
- You may freely distribute the URL identifying the publication in the public portal

If you believe that this document breaches copyright please contact us providing details, and we will remove access to the work immediately and investigate your claim.

# Engineering of Electromechanical Oxides by Symmetry Breaking

Haiwu Zhang, Milica Vasiljevic, Achilles Bergne, Dae-Sung Park, Andrea R. Insinga, Shinhee Yun, Vincenzo Esposito, and Nini Pryds\*

Complex oxides exhibit a wide range of fascinating functionalities, such as ferroelectricity, piezoelectricity, and pyroelectricity, which are indispensable for cutting-edge electronics, energy, and information technologies. The intriguing physical properties of these complex oxides arise from the complex interplay between lattice, orbital, charge, and spin degrees of freedom. Here, it is reviewed how electromechanical properties can be achieved/improved by artificially breaking the symmetry of centrosymmetric oxides via engineering thermodynamic variables such as stress, strain, electric field, and chemical potentials. The mechanisms that have been utilized to break the inherent symmetry of conventional materials that lead to novel functionalities and applications are explored. It is highlighted that access to “hidden phases,” which otherwise are prohibited, could uncover opportunities to host exotic properties, such as piezoelectricity, pyroelectricity, etc. This review not only reports how to engineer intrinsically nonpolar and centrosymmetric oxides for emergent properties, but also has implications for manipulating polar functional materials for better performance.

understanding of the structure-properties relationships that arise because of symmetry breaking.

Interfaces are of particular importance here since, by definition, they break the inherent inversion symmetry of a system, thus promoting unique and new properties and metastability.<sup>[2]</sup> The substantial progress in oxide thin-film growth whereby the interface can be controlled at the atomic scale, has accelerated the study of interfaces and their effects. In oxide materials such as transition metal oxides (TMOs), the symmetry of the order parameter is fundamental to observing and understanding new and exotic physical properties. In such materials, the electronic and structural reconstructions at interfaces of dissimilar oxides are driven primarily by electrostatic and strain-related effects. Therefore, understanding the formation and collapse process of symmetry is of significant interest in the basic science of TMOs.


As Landau recognized many years ago, the essence of phase transitions is the breaking of symmetry. A particularly interesting material class with respect to symmetry breaking is ferroelectric materials, where the symmetry breaking is captured by the order parameter called spontaneous polarization. This behavior is most prominent in the solid solution of lead magnesium niobate with lead titanate (e.g.,  $\text{PbMg}_{1/3}\text{Nb}_{2/3}\text{O}_3\text{-PbTiO}_3$ , PMN-PT), in which the best performance is observed at the morphotropic phase boundary.

One of the characteristic features of ferroelectrics is the transition from a high-temperature, centrosymmetric paraelectric phase (PE) to a low-temperature, low-symmetry ferroelectric phase (FE) in the vicinity of the Curie temperature ( $T_c$ ). Such a paraelectric-to-ferroelectric phase transition normally leads to a small structural distortion but a notable symmetry change. The phenomenon by which some symmetrical elements of the paraelectric phase are absent in the FE is an example of what is known as symmetry breaking. Another well-known ferroelectric material is  $\text{BaTiO}_3$  (BTO), which exhibits a series of phase transitions upon cooling from high temperature, that is, cubic ( $Fm\bar{3}m$ )  $\rightarrow$  tetragonal ( $P4mm$ )  $\rightarrow$  orthorhombic ( $Amm2$ )  $\rightarrow$  rhombohedral ( $R3m$ ). The transition from the centrosymmetric cubic phase to the tetragonal phase is accompanied by the emergence of ferroelectric polar ordering, which is prohibited in the high

## 1. Introduction

Breaking the crystal symmetry of materials is of fundamental importance and has received considerable attention for generating emergent phenomena across nearly all scientific disciplines. For example, biology, magnetism, superconductivity, ferroelectricity, and cell movement are just a few representative examples where symmetry and symmetry breaking play a major role.<sup>[1]</sup> In the field of condensed matter physics, phase transitions of materials is an active area of study. They occur in a wide variety of systems and are driven by the breaking of crystal symmetries. Studying these transitions requires a fundamental

H. Zhang, M. Vasiljevic, A. Bergne, D.-S. Park, A. R. Insinga, S. Yun, V. Esposito, N. Pryds  
 Department of Energy Conversion and Storage  
 Technical University of Denmark (DTU)  
 Fysikvej 1, B310, 2800 Kgs. Lyngby, Denmark  
 E-mail: nipr@dtu.dk

 The ORCID identification number(s) for the author(s) of this article can be found under <https://doi.org/10.1002/admi.202300083>.

© 2023 The Authors. Advanced Materials Interfaces published by Wiley-VCH GmbH. This is an open access article under the terms of the Creative Commons Attribution License, which permits use, distribution and reproduction in any medium, provided the original work is properly cited.

DOI: 10.1002/admi.202300083

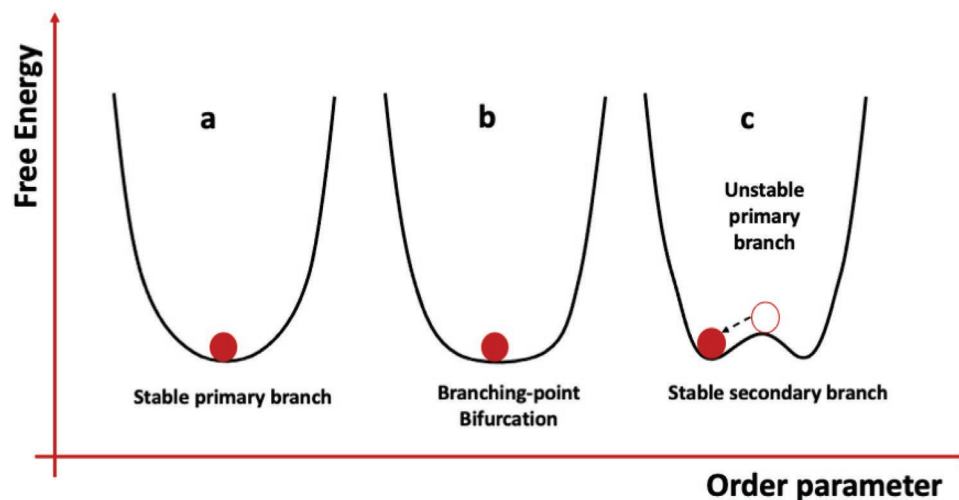


**Figure 1.** Spontaneous symmetry breaking. a) The system has only one stable and symmetric solution for a fixed set of parameters. b) Changes in the local stability properties and c) unstable solution, and the system chooses randomly between two new alternative states, thus, breaking the symmetry.

temperature paraelectric phase. The ferroelectric order parameter is therefore used to measure the degree of order and thereby the symmetry breaking. A schematic characteristic of free energy versus polarization relationship shows the symmetry of a natural ferroelectric ground state with two equal and opposite polarization levels (see schematic illustration in Figure 1).

When the temperature is lowered below the transition temperature, some of the symmetry-imposed restrictions are released, and the system transitions from the PE phase to the FE phase. For example, in BTO, the spatial inversion symmetry breaks due to the off-center motions of  $\text{Ti}^{4+}$  and  $\text{O}^{2-}$  ions (with respect to that of  $\text{Ba}^{2+}$  ions) when the crystal transforms from the cubic PE phase ( $Fm\bar{3}m$ ) to the tetragonal FE phase ( $P4mm$ ).

Piezoelectricity describes the ability of a material to develop electric charge in response to the applied mechanical stress (direct piezoelectric effect) and vice-versa (inverse piezoelectric effect). Symmetry-imposed restrictions on the number of available materials remain a major limitation as 22 out of 32 crystallographic material classes exhibit neither the pyroelectricity nor the piezoelectricity required for ferroelectricity. Yet, by breaking the lattice symmetry, it is possible to circumvent this limitation for example by means of manipulating the charge defect and ultrathin oxide multilayers. Park et al.<sup>[3]</sup> show a way to break the symmetry of centrosymmetric highly oxygen-defective fluorites, for example, gadolinium-doped ceria (CGO), by applying a constant electric field in addition to an alternating field. This turned the electrostrictive CGO into a piezoelectric material by manipulating the mobile charged defects. In another recent work, Zhang et al.<sup>[4]</sup> discovered a new way to tune the electrostriction of oxides via artificial synthesis of heterostructures with alternating layers of CGO and  $\text{Er}_2\text{O}_3$ -stabilized  $\delta\text{-Bi}_2\text{O}_3$  (ESB). They found that the electrostriction in such heterostructures can be engineered by the interfacial lattice discontinuities, which yield an electrostriction coefficient being three orders of magnitude larger than the best-known relaxor ferroelectrics (e.g., PMN-PT). This work thus opens a new avenue

for the design and manipulation of electrostrictive materials by interfacial engineering.

Oxide surfaces are another example that received relatively little attention although they have been shown to exhibit large polarity owing to the surface broken symmetry. Meirzadeh et al.<sup>[5]</sup> show that despite the fact that bulk  $\text{SrTiO}_3$  (STO) is not pyroelectric, the (100) surface of  $\text{TiO}_2$ -terminated STO is intrinsically pyroelectric at room temperature. The pyroelectric effect is a change in surface charge (capacitance) in response to a change in temperature. The pyroelectric active layer is found to be  $\approx 1$  nm thick and, surprisingly, its polarization is comparable with that of strongly polar materials such as BTO. These findings may pave the way for tailoring piezo- and pyroelectric materials through appropriate breaking of symmetry at surfaces and at artificial nanostructures such as heterointerfaces and superlattices.

Here, we review the topics that have been in the spotlight of scientific interest recently, where the symmetry of ferroelectric, piezoelectric, electrostriction, and pyroelectric materials manifests itself in surfaces, interfaces, strain gradients, chemical engineering, and electronic/ionic structures. This review article is dedicated to symmetry and symmetry breaking and is aimed to provide a representative overview of ferroelectric, piezoelectric, electrostriction, and pyroelectric oxide materials, rather than providing an exhaustive account of all studies related to the application of all materials.

## 2. Electromechanics and Symmetry Breaking in Oxides

### 2.1. Theoretical Background

#### 2.1.1. Electro-Elastic Coupling

This sub-section is focused on electro-elastic coupling mechanisms. The following equations can express the relevant constitutive relations:

$$\begin{cases} \sigma_{ij} = C_{ijkl} \varepsilon_{kl} + e_{ijk} E_k + \mu_{ijkl} \partial_k E_l + M_{ijkl} E_k E_l \\ D_i = \varepsilon_{ij} E_j + e_{ijk} \varepsilon_{jk} + \mu_{ijkl} \partial_j \varepsilon_{kl} \end{cases} \quad (1.1)$$

where  $\sigma_{ij}$  is the stress tensor,  $\varepsilon_{kl}$  is the strain tensor,  $D_i$  is the electric displacement field vector,  $E_i$  is the electric field vector,  $C_{ijkl}$  is the stiffness tensor,  $e_{ijk}$  is the piezoelectric coupling tensor,  $\mu_{ijkl}$  is the flexoelectric coupling tensor,  $M_{ijkl}$  is the electrostrictive tensor,  $\varepsilon_{ij}$  is the electric permittivity tensor, and  $\partial_i$  denotes the partial derivative for the  $i^{\text{th}}$  spatial coordinate. The four terms on the right-hand side of the first equation correspond to linear elasticity, piezoelectricity, flexoelectricity, and electrostriction, respectively. The three terms on the right-hand side of the second equation correspond to polarizability, piezoelectricity, and flexoelectricity, respectively.

There are alternative equivalent ways of expressing the same constitutive relations, especially by considering the electric polarization  $P$  which satisfies  $D = \varepsilon_0 E + P$ . For example, the electrostrictive contribution to the stress tensor can be written as  $Q_{ijkl} P_k P_l$ , where  $Q_{ijkl}$  is the electrostriction coefficient.

### 2.1.2. Symmetries and Symmetry Breaking

The crystal structure of a material determines which kinds of electromechanical coupling and polarization can occur in the material. In particular, there are 32 crystal point groups for all crystals and 21 of these are noncentrosymmetric. Among these, only 20 crystal point groups show piezoelectricity. Furthermore, only 10 groups of the 20 piezoelectric point groups possess spontaneous polarization and thus show pyroelectricity. Ferroelectric materials are a subclass of the pyroelectric family exhibiting switchable remanent polarization under external electric field.

By definition, crystal lattices are periodic structures displaying discrete translational symmetry along three independent directions. This property is mathematically expressed by defining three primitive translation vectors  $\{a_1, a_2, a_3\}$ , and requiring that the lattice be invariant with respect to any translation defined as:

$$T = c_1 a_1 + c_2 a_2 + c_3 a_3, \text{ with } c_1, c_2, c_3 \in \mathbb{Z} \quad (1.2)$$

The unit cell is the smallest segment that is repeated along each of the three directions to tile the whole crystal space. There are infinite equivalent alternatives for selecting the unit cell. However, the most natural choice is the parallelogram delimited by the primitive vectors. Due to the requirement of discrete translational symmetry, the classes of compatible discrete rotational symmetries are limited, as expressed by the crystallographic restriction theorem. Indeed, the rotational symmetries allowed for crystals are onefold, twofold, threefold, fourfold, or sixfold, corresponding to rotations by  $360^\circ$ ,  $180^\circ$ ,  $120^\circ$ ,  $90^\circ$ , and  $60^\circ$ , respectively (although for quasicrystals different rotational symmetries are allowed).

A consequence of this theorem is that there are only 32 allowed point groups (the symmetry groups with at least one common fixed point), for 3D crystals. Of these, 27 belong to one of the 7 infinite series of axial groups, that is, characterized

by at most one rotational axis with more than twofold rotational symmetry). The other 5 are polyhedral groups characterized by at least 2 rotational axes with at least threefold rotational symmetry.

The two fundamental principles relating the point group of a crystal with its physical behavior are Neumann's and Curie's principles.<sup>[6]</sup> Neumann's principle states that the tensors describing the macroscopic physical behavior of a material possess at least the same point symmetry groups as the corresponding crystal. Denoting by  $G_T$  the symmetry groups of the tensor, and by  $G_C$  those of the crystal, we have  $G_C \subseteq G_T$ . Curie's principle considers a crystal under the effect of an external effect, represented by a tensor field  $E$ . The symmetry group  $G_{C'}$  of the crystal under the influence of the field is the intersection between the symmetry group  $G_C$  of the unperturbed crystal and the symmetry group  $G_E$  of the external tensor field:

$$G_{C'} = G_C \cap G_E \quad (1.3)$$

These two principles manifest in a wide variety of physical phenomena. Here, we are particularly interested in electric, elastic, and thermal phenomena, and their corresponding couplings.

One important representative case is that the piezoelectric effect cannot be observed for centrosymmetric crystals. The electric dipole moment,  $p$ , of the unit cell  $\Omega$ , with respect to the starting point  $x$ , is related to the electric charge density  $\rho$  by:

$$p(x) = \int_{\Omega} dV \rho(x') (x' - x) \quad (1.4)$$

For an electrically neutral crystal (i.e., satisfying  $\int_{\Omega} dV \rho(x') = 0$ ) the starting point  $x$  is irrelevant, so we choose the origin  $x = 0$ . It is convenient to define the unit cell so that it is symmetric with respect to the origin:

$$\Omega = \{x : x = u_1 a_1 + u_2 a_2 + u_3 a_3, \text{ with } u_1, u_2, u_3 \in [-1/2, +1/2]\} \quad (1.5)$$

Since the uniaxial strain satisfies inversion symmetry, and we assume that the unperturbed crystal does too, Curie's principle states that the crystal under the effect of the external strain will be centrosymmetric as well. Therefore, the corresponding charge density function satisfies  $\rho(x) = \rho(-x)$ . The electric moment is thus obtained as the integral of an anti-symmetric function over a symmetric set, thus leading to  $p = 0$ . In a piezoelectric material, a uniaxial strain would cause an electric polarization. Therefore, a material with a centrosymmetric crystal structure cannot be electrically polarized under an external strain, that is, it thus cannot exhibit piezoelectric behavior.

Of the 32 crystallographic point groups, 21 are non-centrosymmetric.<sup>[7]</sup> Among these, 10 are polar and have more than one point that is invariant under every symmetry operation of the crystal. Conversely, for nonpolar point groups, all the fixed points are invariant under all the symmetry transformations of the group. Since the symmetry operations are linear, the set of fixed points is necessarily a vector space. Polar point groups, which cannot be centrosymmetric, have a lower symmetry than non-polar ones.

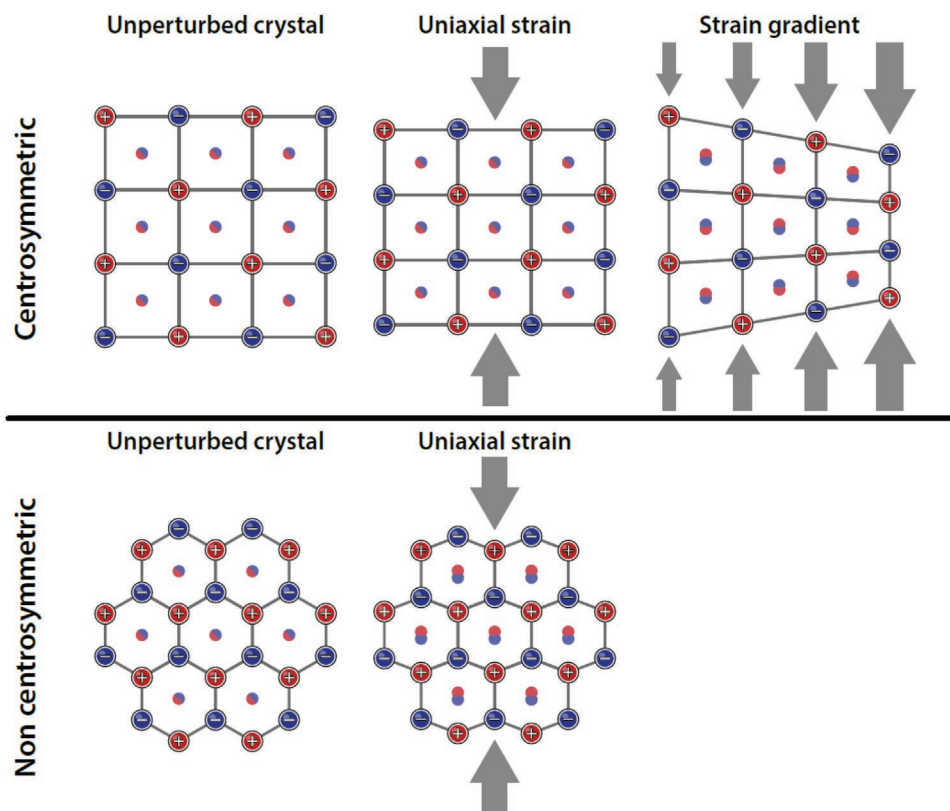


**Figure 2.** Illustration of symmetry breaking mechanism and the possible emergence of electric polarization. The red and blue circles indicate positive and negative ions, respectively.

Neumann's principle predicts that polar crystals are the only class of materials that can exhibit spontaneous polarization. For spontaneous polarization, even if the material is not under the influence of any external field, the electric dipole moment vector  $p$  adopts the same symmetries as the crystal itself, which is impossible for the nonpolar case. To see this effect, let us consider a crystal that is symmetric with respect to a transformation  $R$ . The vector  $p$  must also be invariant under any symmetry transformation of the crystal, so it must be an element of  $\Omega_0$ . If the crystal is nonpolar, there must be at least one different transformation  $R'$ , which does not leave  $\Omega_0$  fixed. In this situation, the polarization cannot satisfy  $R'p = p$ , and the vector  $p$  would thus not be invariant under all the symmetry transformations of the crystal, which would violate Neumann's principle. Materials exhibiting spontaneous polarization also display pyroelectric behavior since the polarization is affected by the temperature.

Considering Curie's principle, the application of an external strain can break the symmetry, which prevents a non-polar material from polarizing. Using strain gradients is another approach to break the symmetry and induce electric polarization due to the flexoelectric effect (see Figure 2).

Figure 2 represents a schematic illustration of the symmetry-breaking mechanisms associated with applying external strain fields. The three top panels show a centrosymmetric crystal, while the bottom panels show a non-centrosymmetric one. Applying a uniaxial strain is sufficient to cause a non-centrosymmetric crystal to be electrically polarized, but it is not

sufficient for a centrosymmetric crystal. On the other hand, a strain-gradient can induce a non-zero net polarization in any material. Similarly, since the electric field is a polar vector, any material can develop polarization under its effect.

By systematically applying Curie's principle and considering the symmetries of its crystal structure, it is possible, for any material, to predict which entries of the coupling tensors (Equation (1.1)) will vanish.

### 2.1.3. Modeling Electromechanical Oxides

In this section, we discuss both analytical and numerical modeling frameworks. Several approaches have been employed to study the emergence of electromechanical and thermoelectrical phenomena due to symmetry reduction caused by a variety of factors. The most suitable modeling framework is usually selected depending on the scale under consideration and the purpose of the investigation.

*Density Functional Theory and Molecular Dynamics:* The Kohn and Sham framework is the foundation for the density functional theory (DFT) simulations.<sup>[8]</sup> This approach considers the exact solution, that is., the wave function, for a reference system of non-interacting electrons subject to an effective potential that would result in the same electron density as the original system of interacting electrons. While the Hartree–Fock method consists of calculating the many-body wave function for a system of electrons, in DFT the total electron density is considered.

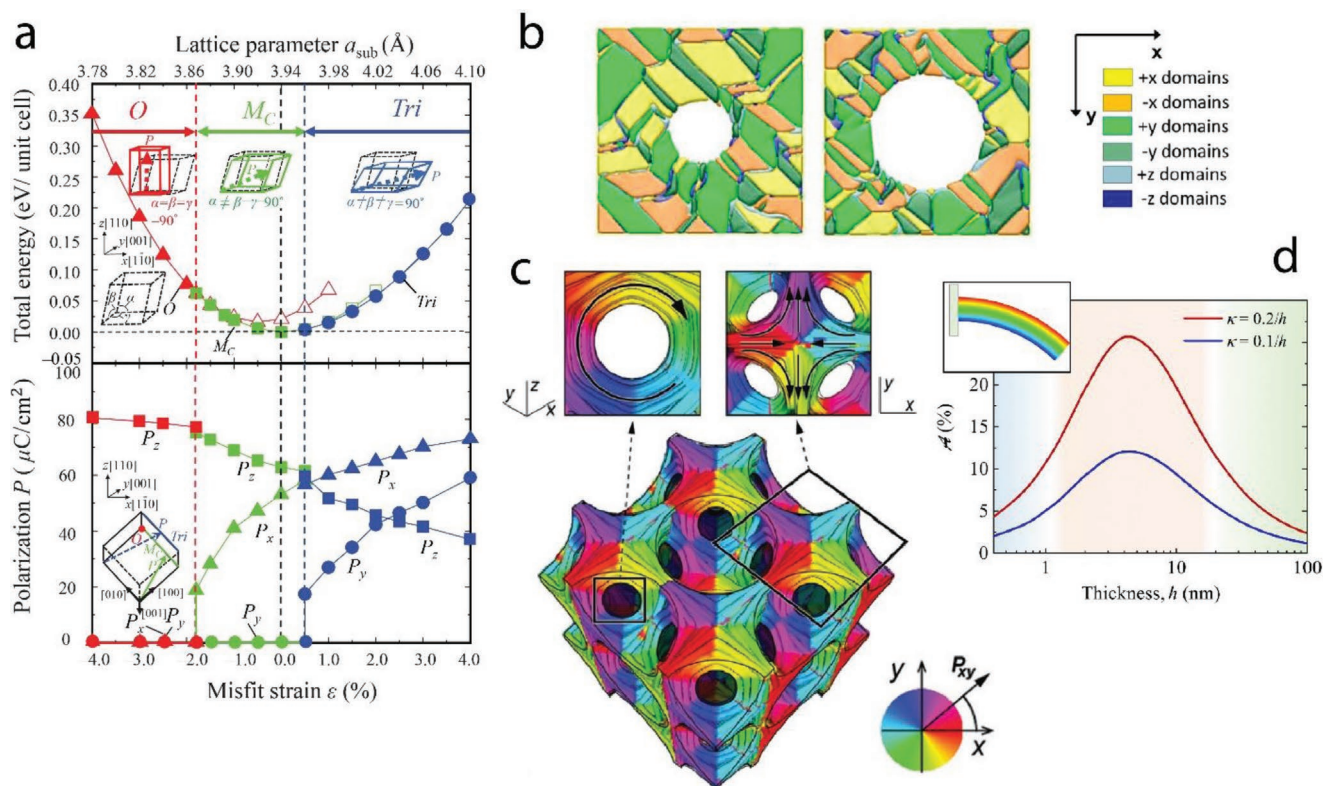


**Figure 3.** Different modeling results. a) Energy and polarization as a function of the strain or the lattice parameter, as predicted by a DFT model. Reproduced with permission.<sup>[14]</sup> Copyright 2015, American Physical Society. b) Ferroelectric domains around a circular defect, computed by PF approach. Reproduced with permission.<sup>[20]</sup> Copyright 2021, Taylor & Francis Group. c) Polarization structure in nanoporous ferroelectric, computed by PF approach. Reproduced with permission.<sup>[21]</sup> Copyright 2017, Royal Society of Chemistry. d) Asymmetric bending rigidity as a function of the cantilever's thickness, analyzed with the linear formalism. Reproduced with permission.<sup>[25]</sup> Copyright 2022, Elsevier.

However, since Kohn and Sham's formalism considers wave functions and not just the electron density, it is possible to construct hybrid approaches combining the Hartree-Fock method with DFT.

Thanks to this approach, the accuracy of the model can be greatly improved. One of the main challenges of DFT approaches is calculating the exchange and correlation energies. The issue is addressed by a family of methods known as generalized gradient approximations<sup>[9]</sup> in which these energy density functionals are assumed to be dependent solely on the local electron density and its gradient. Different expressions for the energy functionals have been proposed, the most widely used being the Perdew-Burke-Ernzerhof (PBE) functional.<sup>[10]</sup>

Lin et al.<sup>[11]</sup> employed DFT to demonstrate that point defects, that is, oxygen vacancies, can be deliberately introduced into SrTiO<sub>3</sub> and SrRuO<sub>3</sub> heterostructures to break the inversion symmetry of the crystal. A ferroelectric behavior can thus be induced in superlattices composed of non-ferroelectric materials. Bare et al.<sup>[12]</sup> have applied DFT in combination with machine-learning models to automate the discovery of new candidate materials for thermochemical hydrogen production. Here, a Monte Carlo "rattling" step is introduced in the calculations to correctly model symmetry-breaking effects due to the oxygen vacancies in perovskite geometries. The physical properties investigated here are the reduction of enthalpy and

entropy as well as the electron-effective mass since these are relevant to solar thermochemical hydrogen production.

Fiete and Rüegg investigated the time-reversal symmetry breaking in thin film oxide heterostructures by combining DFT and HF methods.<sup>[13]</sup> Xu et al.<sup>[14]</sup> applied a hybrid functional of Hartree-Fock and density-functional theory to demonstrate the simultaneous emergence of ferroelectricity and anti-ferromagnetism in multifunctional oxides, which arises from the interaction between oxygen vacancies and epitaxial strains, see Figure 3a. Alaria et al.<sup>[15]</sup> used DFT to study the engineered spatial inversion symmetry breaking in LaFeO<sub>3</sub> and YFeO<sub>3</sub> heterostructures and to predict their magnetic, ferroelectric, and piezoelectric behaviors.

Molecular dynamics simulations are another computational approach that can predict the behavior of a relatively large collection of molecules in a material. It can be used to simulate the time-evolution of each molecule where the interactions between the molecules are described by force-fields. The laws of mechanics used are generally Newtonian, although the functional forms for the force fields can be obtained from quantum mechanical considerations. However, there are also quantum molecular dynamics approaches<sup>[16]</sup> that evolve the quantum probability current of each molecule. Zhao et al.<sup>[17]</sup> considered finite temperature DFT molecular dynamics to investigate the role of intrinsic and thermally induced symmetry breaking on the electric properties of oxide and halide cubic perovskites.

*Phase Field Models:* The HF and DFT methods are typically limited to small systems that contain less than one hundred atoms. Alternative approaches are needed for medium- and large-scale simulations. For example, phase field (PF) simulations are one of the methods employed on this scale. Here, quantum effects may be included in a semiclassical phenomenological fashion as additional terms in the free energy functional that govern the time-evolution of the system.

Specifically, in PF models, one predicts the evolution of one or more space-dependent order parameters that describe the relevant physical mechanisms. Typically, the electric polarization density is the order parameter underlying materials' electromechanical and thermoelectrical behavior. The corresponding theory is known as the Landau–Ginzburg–Devonshire theory.<sup>[18]</sup> The functional derivative of the free energy functional with respect to the order parameter is derived using variational calculus. This derivative appears in the Ginzburg–Landau equation, which describes the system's relaxation toward equilibrium states, that is, the configurations that minimize the free energy.

PF models study the emergence of polarization structures (e.g., vortices) and the motion of ferroelectric domains. For example, Zhu et al.<sup>[19]</sup> analyzed the symmetry-breaking effects occurring on the surfaces of a ferroelectric crystal and their influence on the electrocaloric behavior of the material. Xie et al.<sup>[20]</sup> investigated the symmetry breaking induced by ellipse-shaped pores in nanoporous barium titanate and the resulting enhancement in the ferroelectric response. Two examples of the domains around a circular pore are shown in Figure 3b. Also, Van Lich et al.<sup>[21]</sup> considered nanoporous ferroelectrics and used a PF model to study the geometrical frustration and emergence of nontrivial topological polarization structures due to surface effects associated with the pores. An example is shown in Figure 3c. Simons et al.<sup>[22]</sup> simulated the interplay between domain structures and grain boundaries in BaTiO<sub>3</sub> and the resulting symmetry-breaking strain fields.

*Linear Formalism:* At the macroscopic scale, when the material can be treated as a continuum, linear models provide a sufficiently realistic formalism. The starting point is again the functional expression of the system's free energy, as in PF models. However, in linear formalism, it is typical to consider only the classical macroscopic contribution to energy. For purely electrostatic systems, the energy density is given by half of the scalar product between the electric field and the electric displacement field. These are assumed to be linked by a linear relation, that is, expressed by a rank-2 tensor. By introducing the electric potential, variational techniques can obtain the equilibrium equation, that is, Gauss's law, and the corresponding boundary conditions. An analogous procedure can be used to obtain the equilibrium equations of linear elasticity.<sup>[23,24]</sup> By introducing additional terms, it is possible to include different coupling effects and higher-order mechanisms.

In particular, the linear formalism has been widely applied to study the interplay between piezoelectricity, flexoelectricity, and surface effects.<sup>[23,25,26]</sup> As mentioned earlier, flexoelectricity breaks the symmetry that would otherwise prevent centrosymmetric crystals from exhibiting an electromechanical coupling mechanism, that is, piezoelectricity. Maranganti et al.<sup>[23]</sup> employed linear theory to derive Green's functions for the

piezo-flexoelectric governing equations. Green's functions can be thought of as the formal solution to the equilibrium equation for the case of a point source. By integrating Green's functions, it is possible to calculate the solution for an arbitrary source. This approach is made for the case of inclusions embedded in a uniform medium, such as a spherical defect in an otherwise homogeneous flexoelectric material.

Lun et al.<sup>[25]</sup> applied the same formalism to predict the behavior of a flexoelectric cantilever composed of BiFeO<sub>3</sub>, and analyzed it in the pure bending mode. They conclude that the resulting asymmetric mechanical properties can only be explained by the interplay between piezoelectricity and flexoelectricity, as shown in Figure 3d. In similar studies on different geometries, the authors highlight that the flexoelectric effect is dominant at the nanoscale when the strain gradients are more intense.<sup>[26]</sup>

## 2.2. Electromechanics in Oxygen-Deficient Oxides

Atomic point defects such as antisite, vacant, interstitial defects, and their clusters induce local crystal lattice distortions, within the host crystal lattices.<sup>[27–29]</sup> The introduction of a point defect thus generates elastic stress and strain fields in the crystal volume surrounding the defect, introducing defect-driven local symmetry-breaking effects.<sup>[30]</sup> Defect-mediated electro-chemomechanical interactions have led to intriguing functional properties such as incipient ferroelectricity and flexoelectricity.<sup>[31–33]</sup> For the last decades, it has been shown that such point defects play a crucial role in creating electromechanical properties in intrinsically non-piezoelectric/non-ferroelectric materials. Some examples include oxygen-reduced perovskites (e.g., SrTiO<sub>3-x</sub>),<sup>[34–36]</sup> metal oxides (e.g., TiO<sub>2-x</sub>), Li-ion systems,<sup>[37]</sup> and ionic conductors (e.g., YSZ, and doped CeO<sub>2-x</sub>).<sup>[38,39]</sup> Since, in oxides, the introduction of oxygen vacancy defects increases lattice volume,<sup>[34,40,41]</sup> the effects of ionically active point defects are remarkably evident in the material's dimension and the charge state of the host oxide ions. It has been reported that large strains of 1–10% in oxides can be induced by introducing oxygen vacancies where the effect is greater than in a conventional field-driven piezoelectric strain of 0.1%.<sup>[41–43]</sup> The oxygen vacancy ( $V_{\text{O}}$ ) is an active ionic defect in the presence of an external electric field application. This mechanism reveals that symmetry breaking in such oxides can be induced by controlling defect dynamics and redistribution under various driving external stimuli.

Hence, defect-mediated symmetry breaking can be crucial in tuning the electromechanical properties and is even more pronounced in oxygen-defective metal oxides. For instance, fluorite-based crystalline materials have the general chemical formula AB<sub>2</sub> (A = Ba, Ca, Hf, Zr, Ce, while B = F, O) and have wide technological applications, such as fuel cells, electroceramics, thermal coatings, oxygen sensors, and exhaust reducers.<sup>[44–48]</sup> Despite their simple crystallographic structure, fluorites remain the subject of much academic research and recent unexpected scientific discoveries such as  $V_{\text{O}}$ -mediated/enhanced ferroelectricity, for example, in HfO<sub>2</sub>-based thin films,<sup>[49–51]</sup> or exceptionally large electrostriction and giant piezoelectric effect, for example, in (Nb,Y)-stabilized Bi<sub>2</sub>O<sub>3</sub> and

acceptor-doped  $\text{CeO}_{2-x}$ .<sup>[3,52,53]</sup> Recently, the development of such materials exhibiting exceptionally large strain in the presence of external electric fields has received tremendous attention for their potential applications in actuators and sensors.

### 2.2.1. Electrostriction in Linear and Non-Linear Dielectrics

Two well-studied basic electromechanical properties are piezoelectric and electrostrictive effects. Piezoelectricity occurs only in non-centrosymmetric materials (20 crystallographic point groups), while electrostriction occurs in all dielectric materials regardless of crystal symmetry (all 32 crystallographic point groups).<sup>[54]</sup> Electrostriction is a common property of dielectric solids, which change their shape in response to an external electric field.<sup>[55,56]</sup> The positive or negative sign of the electrostriction coefficient corresponds to the material's expansion or contraction. The field-induced electrostrictive strain for conventional inorganic electrostrictors (e.g., PMN and PMN-PT) manifests itself by an expansion along the direction of external electric fields.<sup>[56]</sup> By contrast, polymers (e.g., vinylidene fluoride-trifluoroethylene) often show compressive strain.<sup>[57,58]</sup> Electrostriction in conventional centrosymmetric materials is hysteresis-free, and thus it is of interest for actuating applications which desire low hysteresis electromechanical coupling, unlike in hysteretic ferroelectricity/piezoelectricity. Further, in ferroelectrics, electrostriction is important for strain engineering, and can have major effects on the Curie temperature, polarization, and phase transitions.<sup>[55,56]</sup>

Contrary to piezoelectrics that have a linear electromechanical response to the electric field, the electrostrictive strain is quadratically proportional to the applied electric fields or dielectric permittivity described as  $x_{ij} = M_{ijkl}E_kE_l = Q_{ijkl}P_kP_l$ .<sup>[55,59]</sup> The  $M_{ijkl}$  and  $Q_{ijkl}$  are the electric field-induced and polarization-induced electrostriction coefficients, respectively. The two coefficients are related by the dielectric permittivity as  $M = Q\varepsilon^2$ , where  $\varepsilon$  is the permittivity of a material. In an empirical law, R. E. Newnham formulated the relationship between electrostriction and dielectric properties for classical electrostrictors such as linear dielectrics (e.g.,  $\text{MgO}$ ,  $\text{SiO}_2$ ,  $\text{TiO}_2$ ), perovskite ferroelectrics (e.g.,  $\text{BaTiO}_3$ ,  $\text{PbTiO}_3$ ,  $\text{Pb}(\text{Ti}_{1-x}\text{Zr}_x)\text{O}_3$ ), and ferroelectric relaxors (e.g.,  $\text{BaTi}_x\text{Sn}_{1-x}\text{O}_3$ ,  $\text{Pb}(\text{Mg}_{1/3}\text{Nb}_{2/3})\text{O}_3$ - $\text{PbTiO}_3$ ).<sup>[59]</sup> Newnham's law relates the electrostriction coefficient ( $Q$ ) with the dielectric permittivity and their elastic properties (compliance,  $s = 1/\text{elastic modulus}$ ) as  $|Q| \approx 2.37 \cdot (s/\varepsilon_0\varepsilon_r)^{0.59}$ , where  $\varepsilon_0$  and  $\varepsilon_r$  are the vacuum permittivity and the relative permittivity of a dielectric material, respectively. The field-induced electrostrictive effect is usually very small compared to piezoelectric effects.<sup>[56]</sup> However, exceptionally large electromechanical properties ( $|M| \approx 5\text{--}100 \times 10^{-18} \text{ m}^2 \text{ V}^{-2}$ ) have been found in oxygen-defective metal oxides such as Gd-doped  $\text{CeO}_{2-\delta}$ , (Nb,Y)-stabilized  $\text{Bi}_2\text{O}_{3-\delta}$  and  $\text{BaCeO}_{3-\delta}$  with intrinsic permittivity of  $\varepsilon_r \approx 20\text{--}40$  and  $Q$  coefficients in the range of  $\approx 40\text{--}300 \text{ m}^4 \text{ C}^{-2}$ .<sup>[3,60-62]</sup> These materials do not obey the empirical Newnham's relation ( $|M|$  or  $|Q|$  versus  $s/\varepsilon$ ), and their electrostriction coefficients are three orders larger than values for typical perovskites including  $\text{SrTiO}_3$ ,  $\text{BaTiO}_3$ ,  $\text{PbTiO}_3$ ,  $\text{Pb}(\text{Ti}_{1-x}\text{Zr}_x)\text{O}_3$ , and  $\text{Pb}(\text{Mg}_{1/3}\text{Nb}_{2/3})\text{O}_3$ - $\text{PbTiO}_3$  ( $Q \approx 0.02\text{--}0.07 \text{ m}^4 \text{ C}^{-2}$ ).<sup>[59]</sup>

The oxygen-defective materials having both large electro-mechanical coefficients and low permittivity are regarded as a new class of electrostrictors – similar features were observed in polymer composites, protonated metal oxides, and lead halide perovskites.<sup>[59,62-64]</sup> There is a remaining debate on the sign of field-induced electrostrictive strain in oxygen-defective oxides. For example, the sign of the field-induced strain was proposed to be negative (i.e., contracts along the direction parallel to the electric field applied) with an oxygen vacancy-mediated lattice contraction (electrostatic interactions).<sup>[52]</sup> By contrast, notable chemical expansion in the defective oxygen ceria was found with different  $V_{\text{O}}$  contents.<sup>[65,66]</sup> The latter was explained by a change in the effective cation radius thanks to the electronic contributions of oxygen vacancies to the surrounding host cations (steric effects). This is a much larger contribution than the effect of oxygen vacancies themselves.

The role and the field-driven dynamics of  $V_{\text{O}}$  defects in electrostrictors are paramount for controlling the associated electromechanical properties. We review here examples demonstrating the tunability of giant electrostriction via intrinsic factors such as the  $V_{\text{O}}$ -mediated atomistic configuration,  $V_{\text{O}}$  concentrations, and charge redistribution in the host fluorite oxide lattices. We also review other approaches employed to tune the electrostriction and generate extrinsic electromechanical properties (piezoelectric effects), for example, dopant size, material dimensionality, strain, interfaces, and external electric bias.

### 2.2.2. Effects of Oxygen Vacancies on Electrostriction

For the last decade, experimental and theoretical studies have been conducted to understand the occurrence of electromechanical coupling in the oxygen-defective metal oxides, particularly doped fluorite oxides, that is,  $\text{R}_x\text{Ce}_{1-x}\text{O}_{2-\delta}$  with aliovalent rare earth dopant,  $\text{R} = \text{La}$ ,  $\text{Pr}$ ,  $\text{Gd}$ , and  $\text{Sm}$ . Electrostriction has been observed both in their bulk ceramic and their thin film forms. Extensive work has been conducted to understand the origin of the effect and to control the electrostrictive responses of these materials concerning the effect of dopant, doping/defect concentration, and microstructures (e.g., grain size, grain orientation, and electrodes).<sup>[52,61,67-70]</sup>

The origins of the electromechanical properties of doped ceria have been proposed to be oxygen vacancy ( $V_{\text{O}}$ )-mediated local lattice distortions and their field-induced displacements within the surrounding lattice of atoms. In a local region where the  $V_{\text{O}}$  defect exists along with the parent  $\text{CeO}_2$  lattices, the defect-mediated lattice distortion is spatially coupled with electric dipoles under an external electric field. The defect-induced local lattice strain and its field-driven strain are shown in **Figure 4**.<sup>[70]</sup> In an earlier experiment, a  $V_{\text{O}}$  position along the [111] crystallographic orientation of the cubic fluorite lattice was proposed as a single-cell model for the maximum field-driven lattice displacements, that is, yielding electrostriction by shrinkage of the diagonal  $V_{\text{O}}\text{-Ce-O}^{\times}$  triplet with applied fields. Later, Santucci et al.<sup>[70]</sup> reported that the highest field-induced electrostriction with a longitudinal electrostriction coefficient of  $|M_{33}| \approx 5 \times 10^{-17} \text{ m}^2 \text{ V}^{-2}$  was found in a [100]-oriented CGO film among the measured crystallographic directions ([100], [110], and



[111]), excited by an alternating electric field of  $E_{AC} = \approx 13 \text{ Kv cm}^{-1}$  at 1 Hz. A lattice model for the induced electrostriction was proposed considering the atomic rearrangement of the surrounding cells, for example, four  $\text{Ce}_{\text{Ce}}\text{-7O-V}_\text{O}$  units. However, these proposed models for the field-driven atomic rearrangement are only valid for describing short-range defect dynamics with relatively small  $E_{AC}$  applications ( $< 0.2 \text{ MV cm}^{-1}$ ). All the above experimental studies show that the induced electrostrictive strain results from a contraction response.

Other reports indicate that the level of  $\text{V}_\text{O}$  in undoped ceria exhibits a linear expansion relationship between the lattice parameter and  $\delta$ .<sup>[65]</sup> The intrinsic oxygen vacancies in the fluorite ceria correspond to the thermodynamic partial reduction of surrounding host Ce cations, that is, the formation of two reduced  $\text{Ce}^{3+}$  bound by a  $\text{V}_\text{O}$  in its tetrahedral coordination. The cause of the expansion upon oxygen reduction was proposed to be the cation valence change ( $\text{Ce}^{4+}$  to  $\text{Ce}^{3+}$ ), as the ionic radius of  $\text{Ce}^{3+}$  ( $\approx 114 \text{ pm}$ ) is larger than that of  $\text{Ce}^{4+}$  ( $\approx 97 \text{ pm}$ ). The  $\text{V}_\text{O}$ -induced charge transfer and lower valence states of the host Ce ions were experimentally observed.<sup>[71]</sup> The oxygen reduction in  $\text{CeO}_{2-\delta}$  can be extended to  $\delta = 0.3$  depending on the material preparation conditions, for example, temperature, oxygen partial pressure, and electromagnetic stimuli.<sup>[65]</sup> The cubic fluorite structure (space group:  $Fm\bar{3}m$ ) is conserved at  $\delta \approx 0.2$ .<sup>[65]</sup> Hence, the degree of stoichiometric expansion in  $\text{CeO}_{2-\delta}$  is correlated with the  $\text{V}_\text{O}$  concentration, which is proportional to  $\delta$ . However, the sign discrepancy of the  $\text{V}_\text{O}$ -induced strain in doped fluorites requires further clarification. Compressive strains are usually observed under relatively low fields ( $< 0.1 \text{ MV cm}^{-1}$ ),<sup>[52,61]</sup> whereas chemical expansion effects are observed under high field ( $> 0.2 \text{ MV cm}^{-1}$ ) or at high temperatures ( $400\text{--}1000 \text{ }^\circ\text{C}$ ).<sup>[53,72]</sup> This effect raises questions about the correlations between external electric field strength, oxygen vacancy contents, charge rearrangement, and the induced electromechanical strain in doped ceria and similar fluorite systems. Moreover, a direct electrochemical reduction of cerium oxides from  $\text{CeO}_2$  to  $\text{Ce}_2\text{O}_3$  under negative electrochemical potentials at around 3 V has been found experimentally and computationally.<sup>[73]</sup>

Of particular interest is the strong excitation frequency dependence (e.g., from a few mHz to a few kHz) of the field-induced electrostrictive performance of doped fluorites.<sup>[52,53,72,74,75]</sup> So far, most of the electromechanical properties of doped ceria were found when the driving AC frequency was decreased toward  $f \rightarrow 0 \text{ Hz}$ . It was also found that the frequency-dependent electromechanical properties of all doped fluorites most likely appear regardless of microstructure properties, dopant species, and dopant concentration.<sup>[68,74,75]</sup> The dielectric permittivity employed for deriving the  $Q$  coefficients in literature is the systems' intrinsic permittivity (high-frequency dielectric constant) of  $\approx 20\text{--}30$ .<sup>[52,61]</sup> However, whether the intrinsic permittivity in the low-frequency regime remains consistent under any given external field has not yet been determined. The electrical interaction of the distorted lattices in the oxygen-defective electrostrictors is slower than for conventional electrostrictors/piezoelectrics. Park et al.<sup>[3]</sup> showed the multiple conductivity changes of a CGO film sample, even excited by a very weak  $E_{AC}$  ( $= 0.79 \text{ kV cm}^{-1}$ ) in the range of  $3 \text{ mHz} \leq f \leq 100 \text{ kHz}$ , and an increase in the low-frequency

conductivity with increasing  $E_{AC}$ . This effect indicates the presence of charged species and multiple dielectric relaxations of the system under external electric field application. Furthermore, the Cole-Cole plots for the complex impedance/dielectric permittivity of undoped and doped ceria and similar fluorites often show tails in the low-frequency regime.<sup>[67,76]</sup> This effect, known as Warburg-diffusive impedance, suggests the presence of mobile ionic species through the Nernst layer at the electrolyte-electrodes interface. Similar results are generally registered in oxygen ionic conductors at a low temperature with oxygen-blocking redox electrodes (e.g., below  $300 \text{ }^\circ\text{C}$ ). However, possible oxygen vacancy transport at or near room temperature raises open questions about the role of defect interactions and their mobility in highly defective configurations.<sup>[77]</sup> The low-frequency electromechanical coupling could be associated with the range of charged defect motion and interfacial and chemical interactions. Thus, addressing these correlations and deriving correct electromechanical coefficients is important for understanding and manipulating the giant electromechanical coupling in doped ceria and similar fluorite systems.

### 2.2.3. Electrosteric Distortion in Ceria by Dopants

Symmetry breaking by electrosteric local distortion is one of the most common effects in crystalline materials. Typical examples are punctual defects, where the size and valence of the substitutional or interstitial species can reach a critical concentration affecting the overall symmetry. Such transitions are generally observed for high defect concentrations, close to the solubility limits, where crystals undergo phase transitions. However, as materials get smaller and smaller, that is, in the nanoscale, short-range and long-range broken symmetries get closer, and local distortions in the crystalline structure become dominant, sometimes triggering unexpected reconfigurations in the long-range.<sup>[2]</sup> Additionally, defects can associate in the nanoscale as the influence of punctual defects (e.g., vacancies, interstitials), linear defects (e.g., dislocation, grain boundary), or 2D and 3D Zener's inclusions becomes larger. The consequences of these nanoscale effects in functional metal oxides are often seen in the overall electromechanical properties.<sup>[78]</sup>

One of the most common ways to induce local distortion for functional metal oxides is via oxygen defectivity.  $\text{V}_\text{O}$  defects can substantially affect their local environment and their influence can extend far beyond their nearest neighbors in ultra-thin films and nanoparticles.<sup>[2]</sup> They can have great influence on ferroelectricity,<sup>[79]</sup> ionic diffusion,<sup>[80]</sup> or even within the nanocrystalline bulk where oxygen defects are high-density or are periodically repeated inside the structure.<sup>[81]</sup> The control of vacancy concentrations and configurations in the nanoscale is thus crucial for property design. Aliovalent doping is the most common way to tune the electrosteric distortion of the structure.

This strategy has been extensively analyzed in acceptor-doped ceria electrostrictors. The generation of intrinsic  $\text{V}_\text{O}$  in pure  $\text{CeO}_2$  is typically small ( $\delta < 0.05$ ). This limits the associated electromechanical properties, for example, low electrostriction performance with coefficients of  $|M| < 10^{-18} \text{ m}^2 \text{ V}^{-2}$ . High concentrations of oxygen vacancies in ceria are introduced by incorporating acceptor dopants (e.g., Pr, Gd, and Sm) as the

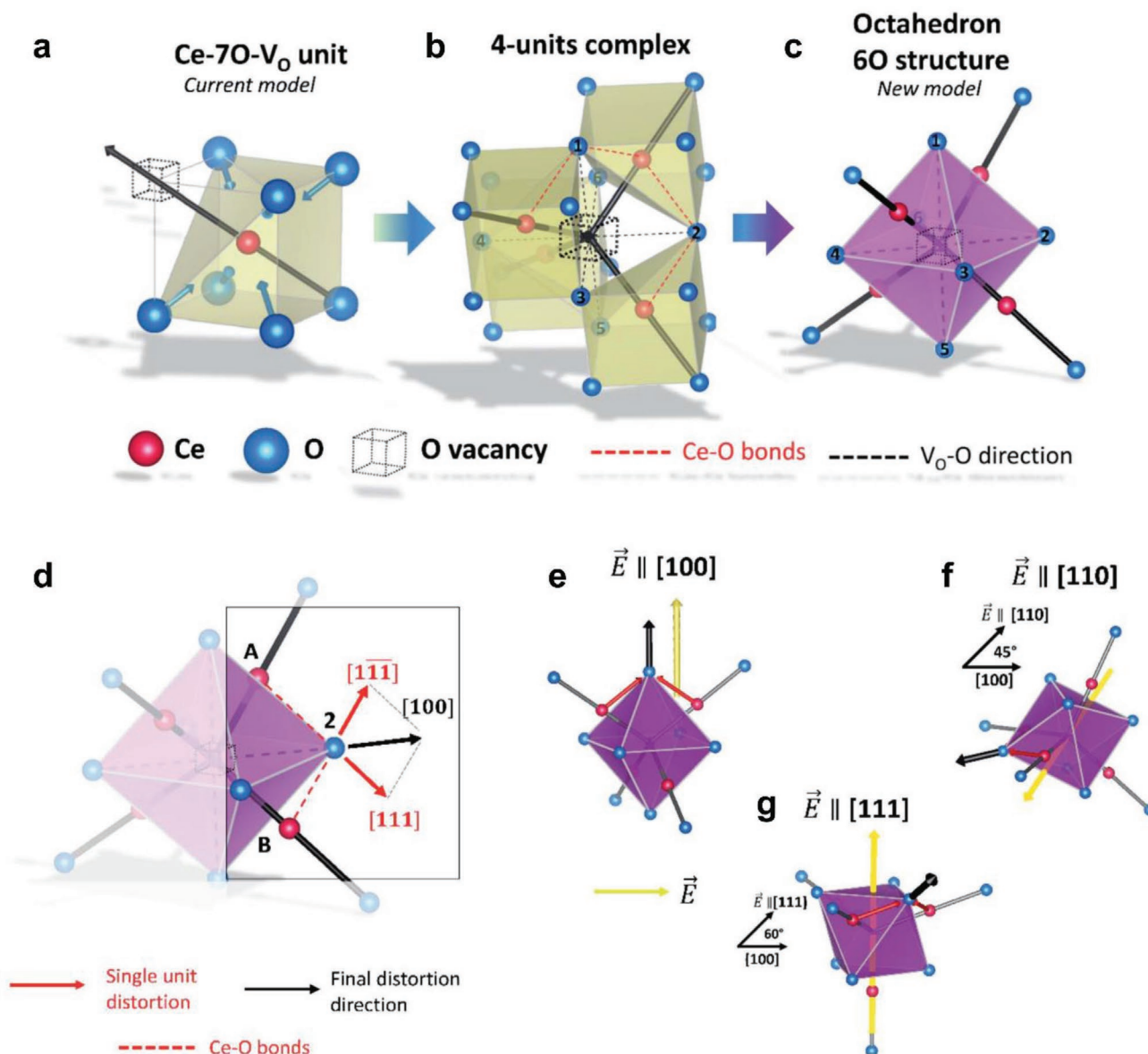


**Figure 4.** Vacancy neighbor structure of CeO<sub>2</sub> and related structures. a) Ce<sub>7</sub>O-V<sub>0</sub> unit, the structure of the model for electrostriction in CGO. Black vector: V<sub>0</sub>-Ce<sub>7</sub>-O<sub>0</sub> electroactive triplet and distortion direction. Blue vectors: consequent 6O displacement b) 4-unit complex composed of four Ce<sub>7</sub>O-V<sub>0</sub> distorted units with central vacancy. Near-empty site oxygen atoms, that is, 6O, are numbered. Red lines highlight the bond direction of Ce ions with oxygen 1 and 2. c) 6O octahedron structure composed of six near-empty site oxygen atoms, base structure for the model proposed by Santucci et al.<sup>[70]</sup> Microscopic interpretation of CGO electrostriction in V<sub>0</sub> neighborhood lattice. d) 4-unit complex with V<sub>0</sub>-Ce<sub>7</sub>-O<sub>0</sub> triplets and imposed stress. e) Preferred direction in octahedron structure parallel with electric field along [100] direction. f) Preferred direction (black line) compared to induced stress with an electric field (yellow line) along [110] with an angle of 45°. g) Preferred direction with electric field parallel to [111] with a 60° angle. Reproduced with permission.<sup>[70]</sup> Copyright 2020, Royal Society of Chemistry.

amount of the vacancy defects are naturally formed to maintain charge neutrality, for example, for the case of Gd<sub>0.2</sub>Ce<sub>0.8</sub>O<sub>1.9</sub> in Kröger-Vink notation,  $Ce_{0.8-2y}^{x}Ce_{2y}^{d'}(Gd'_{ce})_{0.2}O_{1.9-y}^{x}(V_{o})_{0.1+y}$ , where  $2Gd'_{ce} = V_{o}$ .<sup>[82]</sup> **Figure 5** summarizes the experimental results for the electrostrictive performance of doped ceria with various aliovalent cations sizes and the theoretically calculated values for the binding energies of V<sub>0</sub>.<sup>[83–85]</sup> The binding energies of Ce-V<sub>0</sub>, which depend on the dopant size, determine the magnitude of the low-frequency giant electrostriction, that is, larger dopants (Sc<sup>3+</sup>, Mg<sup>2+</sup>, Gd<sup>3+</sup>, La<sup>3+</sup>) give larger electrostrictions.

These results reveal that the ionic radius of the aliovalent cation dopants is an effective parameter to tune the electromechanical properties of ceria-based materials.

Such an aliovalent cation doping in ceria greatly enhances the electrostrictive performance with longitudinal coefficients of  $|M_{33}| = 10^{-18} - 10^{-16} \text{ m}^2 \text{ V}^{-2}$  in the low-frequency regime (<10 Hz).<sup>[75]</sup> However, some studies show no clear correlation between local distortion induced by the V<sub>0</sub> concentration and electrostriction when the V<sub>0</sub> contents are above 20%, where defect ordering leads to a symmetry break from defective

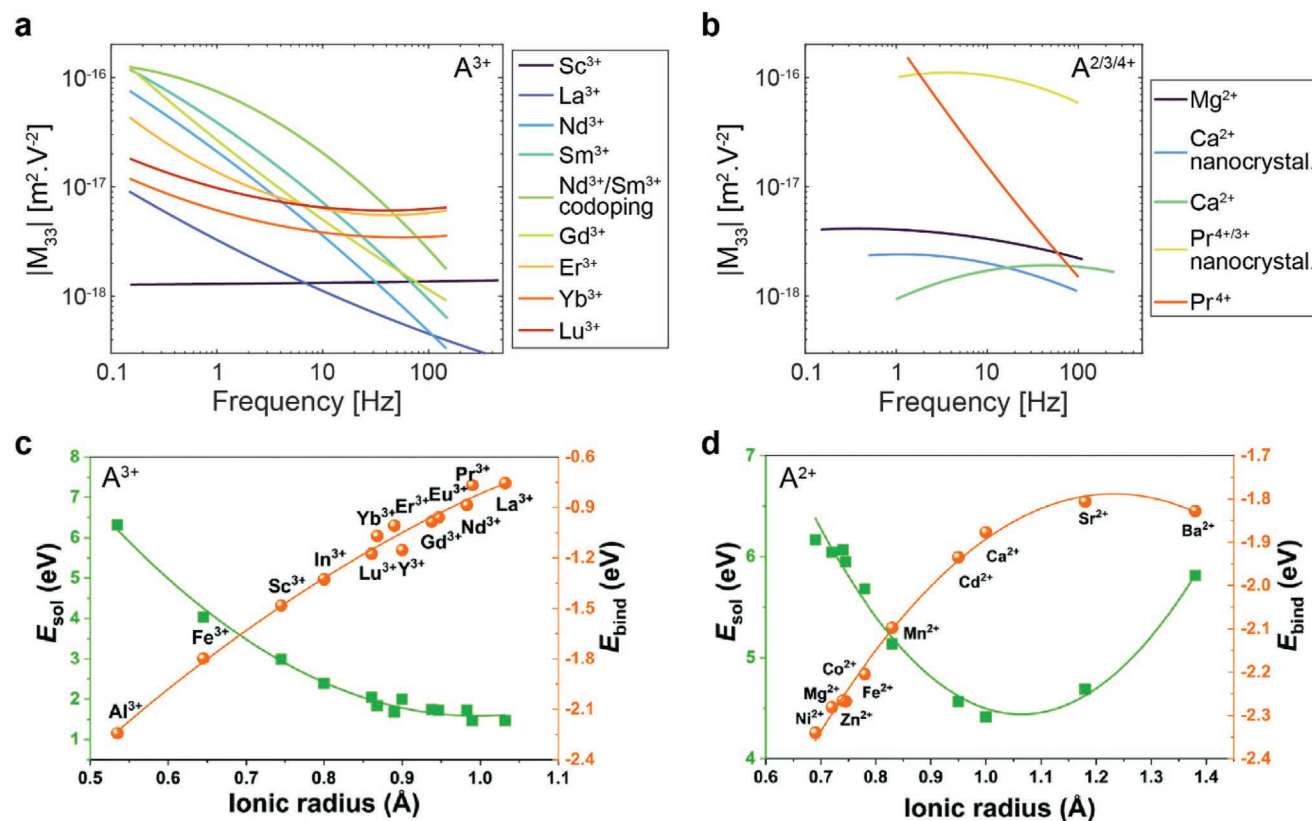


**Figure 5.** Effect of dopant on the electrostriction of CeO<sub>2</sub> solid solutions. a)  $|M_{33}|$  as a function of frequency for 3+ dopants (Nd, Sm, Gd, Er, Yb, Lu data taken from ref. [74] Nd/Sm co-doping data taken from ref. [83] Sc, Lu data taken from ref. [84]). b)  $|M_{33}|$  as a function of frequency for 2/3/4+ dopants (Mg data taken from refs. [3,84]. Ca data taken from ref. [86] Pr data taken from ref. [89]); solution energy and binding energy of c) M<sup>3+</sup> and d) M<sup>2+</sup> cations in CeO<sub>2</sub> solid solutions calculated by atomic scale simulations.<sup>[85]</sup> c,d) Reproduced with permission.<sup>[85]</sup> Copyright 2020, Royal Society of Chemistry.

fluorite to double fluorite. Varenik et al.<sup>[75]</sup> reported that higher  $V_{\text{O}}$  inclusion even degrades the electrostrictive performance in Gd<sup>3+</sup>- and Sm<sup>3+</sup>-doped CeO<sub>2-x</sub> ceramic pellets.

In another paper, Varenik et al.<sup>[74]</sup> investigate the steric effect of substitutional doping on electrostriction. Their results show that aliovalent dopants with different trivalent cation sizes can influence the electromechanical response. The size of trivalent dopants (e.g., Lu<sup>3+</sup>, Yb<sup>3+</sup>, Er<sup>3+</sup>, Gd<sup>3+</sup>, Sm<sup>3+</sup>, and Nd<sup>3+</sup>) vary the electrostriction coefficients by two orders of magnitude from 10<sup>-18</sup> to 10<sup>-16</sup> m<sup>2</sup> V<sup>-2</sup> in the low-frequency regime ( $f < 10$  Hz) (Figure 5). The results show that the steric effect seems to affect the time constants as the electromechanical response strongly depends on the operational frequency of the applied field. Another investigation explored a co-doping effect on the electrostriction of polycrystalline Ce<sub>1-x</sub>(Sm<sub>0.5</sub>/Nd<sub>0.5</sub>)<sub>x</sub>O<sub>2-x/2</sub> ceramics with aliovalent A<sup>3+</sup> cations.<sup>[83]</sup> The effect was driven by simultaneously incorporating dopants with relatively smaller and bigger sizes with respect to the size of host Ce for an undistorted cubic fluorite structure. The averaged grain size became smaller from 5.6 to 2.0 μm when  $x$  was increased. The induced electrostriction ( $|M_{33}| \approx 7\text{--}8 \times 10^{-17}$  m<sup>2</sup> V<sup>-2</sup>) of the co-doped ceramics ( $x \leq 5$ ) in the low-frequency range was two or three times larger than that of a CGO ceramic (with 10% Gd), while the high-frequency  $|M_{33}|$  remained almost constant at  $\approx 2 \times 10^{-18}$  m<sup>2</sup> V<sup>-2</sup>. It was suggested that low  $V_{\text{O}}$  concentrations are necessary for low-frequency electrostriction. A similar

strategy has been used to examine the effect of oxygen vacancy migration in ceria.<sup>[86]</sup> The result confirms that minor lattice distortion limits the electrostriction at lower measurement frequencies. A doped ceria (Ca<sup>2+</sup>-doped CeO<sub>2</sub>, CCO) with low valence and large cation size shows most likely frequency-independent electrostrictive performance ( $|M_{33}| \approx 1 \times 10^{-18}$  m<sup>2</sup> V<sup>-2</sup>) in an operating frequency range (1 Hz–1 kHz range).<sup>[84,86]</sup> Although the induced electrostriction in CCO is smaller than the performance of other doped ceria, the calcium-doped compounds were expected to have a response time faster than milliseconds, making these materials potentially suitable for ultrasonic applications. Nanodomains with broken symmetry have been reported in CCO,<sup>[87]</sup> and they are likely formed in other highly doped ceria solid solutions.<sup>[88]</sup> The presence of extensive nanodomains in CCO is generally attributed to the low valence of the cation, which will tend to segregate and stabilize rather different symmetries.<sup>[87]</sup> Such a feature, would also explain the limited influence of the grain sizes on the electrostrictive performance in the nanocrystalline materials (Figure 5b). Recent results on isovalent-doped ceria, such as Pr<sup>3+/4+</sup>-doped ceria, make the picture even more intriguing and highlight the extended effects of local distortions on the nanocrystalline bulk materials. In such compounds, the oxygen vacancy concentration is directly related to the dominant polaron defects, which also bring large steric effects. Although the concentration of oxygen defects is small, the electromechanical activity

of Pr<sup>3+/4+</sup>-doped ceria remains steady at high frequencies, especially for nanocrystalline materials with higher concentrations of small polarons (Figure 5).<sup>[89]</sup>

#### 2.2.4. Size, Strain, and Interface Effects on Electrostriction

Together with advances in thin film growth techniques, it is possible to design and fabricate synthetic oxide thin films and heterostructures.<sup>[90]</sup> This strategy allows the properties of existing materials to be modified by size-scaling, strain, and interface engineering.

- 1) It is known that ionic motion/deformation can be greatly enhanced by lowering the material's dimensionality due to less stable long-range atomic order.<sup>[91,92]</sup> In bulk systems (3D), atomic displacements are restrained by atoms from all directions, while in the 2D layer, such constraints are weaker or absent.<sup>[91]</sup> Thus, fewer restrictions for atomic displacements can be expected when the thickness of a crystal decreases.
- 2) Epitaxial strain can break the symmetry of centrosymmetric materials and determine the defect configurations in distinct directions along interfaces. Such engineering has already been shown to guide a preferential path for ionic (defect) transport and diffusion effects, for example, using tensile or compressive strain-induced deformations, on an underlying material (in-plane lattice spacing).<sup>[93]</sup> Furthermore, unique and preferential defect arrays in the certain crystallographic directions of strained epitaxial films can be spontaneously formed as a result of the minimization of strain energy.<sup>[94]</sup>
- 3) In atomically engineered heterointerfaces, interfacial effects can lead to the confinement and the enhancement of hopping/diffusion of ions/defects.<sup>[95]</sup> Along with these studies, giant electrostriction was recently found in artificially engineered CGO-based superlattice samples, which combine the effects of low-dimensionality, strain, and interfaces on the defect motion and result in electromechanical coupling.<sup>[4]</sup>

Recently, Zhang et al. demonstrated a new approach to engineering electrostriction through artificial interfaces. It was realized by depositing heterostructures with alternative layers of Gd<sub>2</sub>O<sub>3</sub>-doped CeO<sub>2</sub> (CGO) and Er<sub>2</sub>O<sub>3</sub>-stabilized Bi<sub>2</sub>O<sub>3</sub> (ESB). The total thickness was fixed at ≈17 nm, and the [ESB/CGO] bilayer thickness (*A*) was tuned by adjusting the number of bilayers. The authors found that the electrostriction coefficients increase with the decrease of the [ESB/CGO] bilayer thickness, with the maximized  $|M_{xx}|$  reaching ≈10<sup>-14</sup> m<sup>2</sup> V<sup>-2</sup> at *A* = 2.27 nm (Figure 6). Such extraordinary electrostriction is three orders of magnitude higher than the commercial, toxic lead-based PMN-PT single crystals.<sup>[96]</sup>

Based on a combined experimental and simulation investigation, the authors found that the reduction in bilayer thickness plays a twofold role: it results in stronger lattice distortions and leads to the coexistence of energy-competing local distortions. Therefore, the lattice distortions are easier to switch between different directions in response to the activating electric field, leading to larger  $|M_{xx}|$ . The mechanism is schemati-

cally illustrated in Figure 7.<sup>[97]</sup> Moreover, a systematic investigation on different defective oxide structures (fluorite, perovskite, garnet, and spinel) confirms that the field-induced strain as a function of the bilayer thickness is fully consistent with the “volcano-like” behavior. Such results demonstrated that multilayering is a promising strategy to achieve large electrostriction. These findings pave the way for the possibility of inducing extraordinary electromechanical coupling by engineering low-dimensional materials which combine the effects of defect motion, strain, and interfaces. This also opens a new avenue for designing highly efficient electromechanical thin film materials at the nanoscale.

#### 2.2.5. Field-Induced Piezoelectric Effect in Doped Ceria

In recent decades, many piezoelectric- and ferroelectric-like behaviors in non-piezoelectric/ferroelectric materials have been found. They are based on the existence of bias-induced electrochemical, electromechanical responses and hysteresis loops in materials such as STO, TiO<sub>2</sub>, ionic conductors including Li-ion systems, YSZ, doped ceria, etc.<sup>[34,37,38]</sup> This technology directly reveals that controlling mobile V<sub>O</sub><sup>•</sup> defects is essential to create and manipulate electromechanical properties. Moreover, new functional oxide materials will emerge beyond the classical concepts (a fundamental requirement of non-centrosymmetric crystal structure, atomic displacement in picometer scale, spontaneous polarization, etc.) of conventional piezoelectrics, pyroelectrics, and ferroelectrics. Thus, solid-state ionic dynamics and polarization-associated phenomena can be potentially critical control parameters for bias-controlled phenomena in materials that have non-linear properties and mobile ionic defects (V<sub>O</sub><sup>•</sup>), for example, the field-driven V<sub>O</sub><sup>•</sup> defects in Gd-doped ceria (Figure 8a).<sup>[3,98]</sup>

Park, et al.<sup>[3]</sup> link the V<sub>O</sub><sup>•</sup>-mediated electrostriction to the generation of a piezoelectric effect using Gd-doped CeO<sub>2-x</sub> (CGO) film samples (thicknesses of 1.2–1.8 μm) performed on out-of-plane capacitor geometry (Figure 8b). This work shows strongly rate-dependent V<sub>O</sub><sup>•</sup> contributions to the induced giant electrostriction of CGO films with a large longitudinal electrostriction coefficient,  $|M_{33}| \approx 10^{-17} - 10^{-16} \text{ m}^2 \text{ V}^{-2}$ , when large alternating current (AC) electric fields above  $E_{AC} \geq 0.5 \text{ MV cm}^{-1}$  were applied in a low-frequency range of <1 Hz as shown in Figure 8c. Based on this, Park et al.<sup>[3]</sup> present a way to break the inversion symmetry of the CGO for the generation of piezoelectricity by applying a static DC field. The induced piezoelectric effect was driven by applying a combined electric field (e.g., simultaneous application of a large DC field and a small driving AC field) to the material (Figure 8d). Furthermore, by tuning the relative strengths of the DC ( $E_{DC}$ ) and AC ( $E_{AC}$ ) fields, this work thus provides selective ways to achieve different electromechanical couplings: i) purely first harmonic piezoelectric effect by concurrently applying both a relatively very large  $E_{DC}$  and a small  $E_{AC}$ , ii) purely second harmonic electrostrictive effect by applying a large  $E_{AC}$ , and iii) mixed first and second electromechanical response by applying comparable amplitudes of  $E_{DC}$  and  $E_{AC}$ . By increasing the magnitude of  $E_{DC}$  the strength of the piezoelectric effect (observed  $d_{33}$ ) increases, whereas changing the sign of  $E_{DC}$  changes the sign of the piezoelectric response (from the

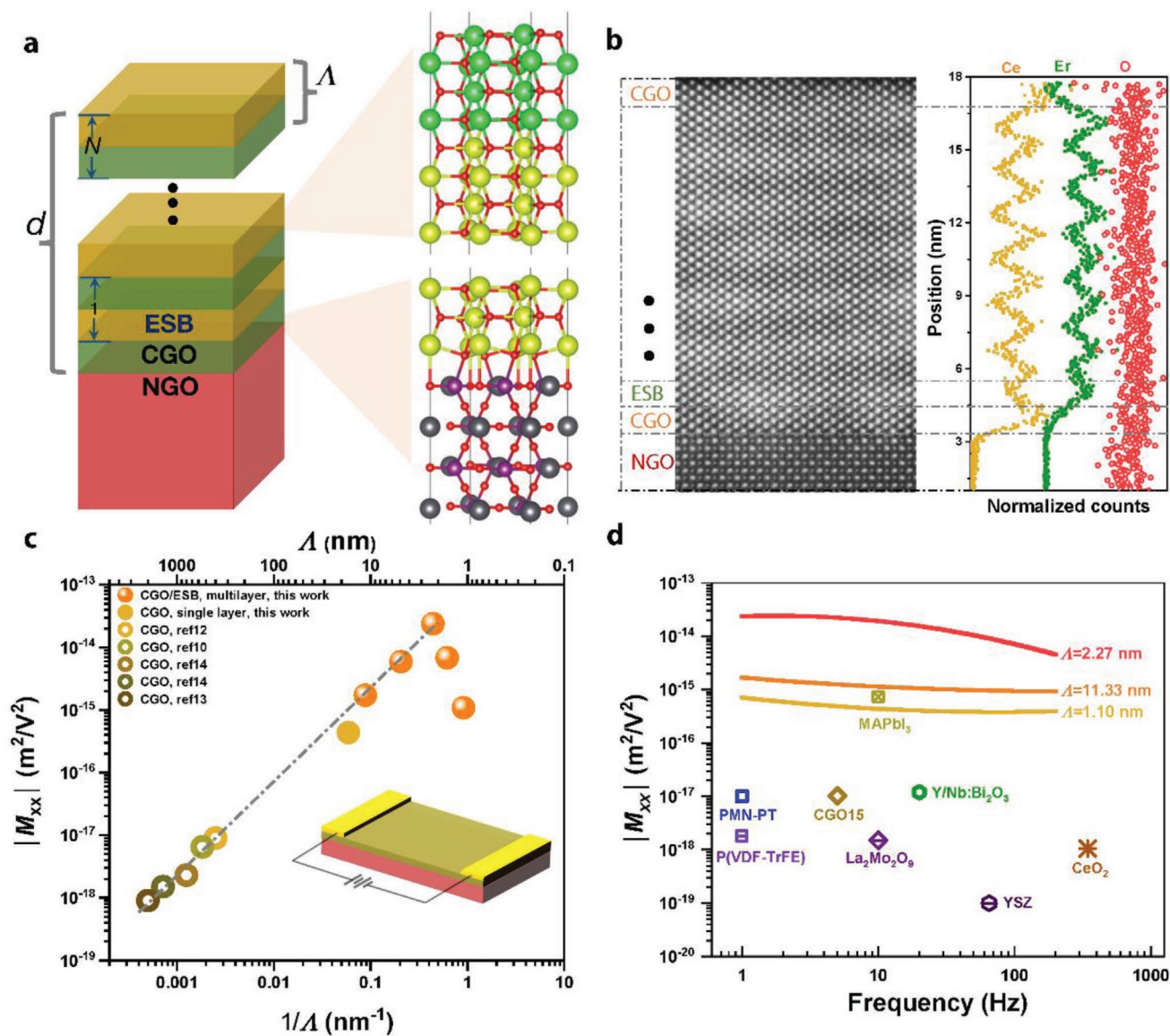


**Figure 6.** Multilayer structure and electrostrictive property of NGO/CGO/[ESB/CGO]<sub>N</sub>. a) Schematic illustration of the multilayer architecture. b) HAADF-STEM image and EDX compositional variations for  $\Delta = 2.27$  nm. c) Electrostriction coefficient ( $|M_{xx}|$ ) as a function of modulation length ( $\Delta$ ) measured at 1 Hz. The inset schematically illustrates the top–top electrode configuration. d) Electrostriction properties of various electrostrictive materials are shown for comparison. Reproduced with permission.<sup>[4]</sup> Copyright 2022, The Authors, under exclusive licence to Springer Nature Limited.

in-phase to out-of-phase) by observing a 180-degree phase shift. This effect confirms the induced first harmonic electromechanical coupling is the piezoelectric effect. The size of the induced apparent piezoelectric effects is about  $d_{33} \approx 200\,000$  pm V<sup>-1</sup> at low frequencies (mHz), which is two orders of magnitude higher than the current best relaxor-ferroelectric, PMN-PT (Figure 8e). Moreover, the induced piezoelectric effect largely sustains at 1 kHz with  $d_{33} \approx 100$  pm V<sup>-1</sup>, comparable to PZT thin films' performance. The same induced effect was found in bulk oxides or thin films, for example, CGO ceramics and YSZ films. This suggests that the high field-induced piezoelectricity could be found in a large class of intrinsically centrosymmetric oxygen-nonstoichiometric fluorite oxides. This work directly shows the impact of the field-driven mobile V<sub>O</sub> defects on the

change of material dimensions by the control of external electric fields.<sup>[3]</sup> Hence, the working concept for the DC field-enforced piezoelectric effect would apply to various centrosymmetric materials not only for extending the range of piezoelectric materials, including pyroelectrics and ferroelectrics but also for their practical high-performance device applications. This work further claimed that under the field applied to the fluorite oxides, the V<sub>O</sub> defect distribution could lead to significant charge redistribution, chemical expansion (e.g., Ce<sup>4+</sup> to Ce<sup>3+</sup>), crystal phase transition, and material heterogeneity.<sup>[3]</sup> These are certainly interesting and important future subjects for understanding the fundamental mechanism and correlation of the induced piezoelectric effects in centrosymmetric materials with mobile ionic defects/species.

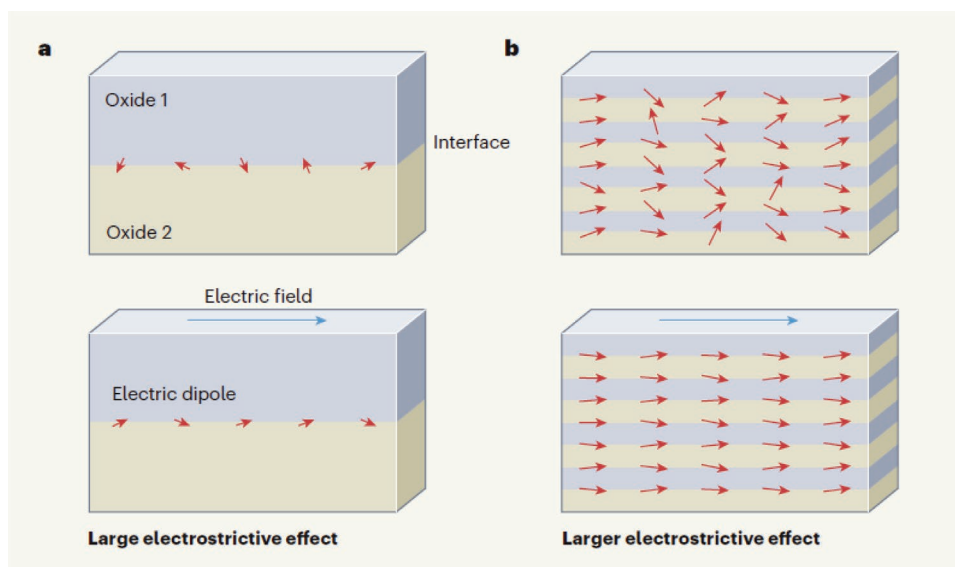


**Figure 7.** Schematic illustration of the mechanism for the extraordinary electrostriction in oxide heterostructures. a) The interfaces induced substantial local distortions, which are easier to be aligned by external electric field. b) Reducing the bilayer thickness enhanced the magnitude of the local structural distortions and dipoles at the interface and thereby increases the magnitude of the electrostriction. Reproduced with permission.<sup>[97]</sup> Copyright 2022, Springer Nature.

### 2.3. Electromechanics at Surfaces and Interfaces

#### 2.3.1. Surface Reconstructions

According to the classical structural model, all perfect ionic crystals can be viewed as stacks of alternating charged lattice planes along certain crystallographic directions. However, in practice, any single crystal inevitably has atomic terminations at the surface, where the electrostatic energy diverges and is compensated in different ways, such as charge transfer, structural reconstruction, polar surface relaxation, etc. This effect results in symmetry breaking and creates unusual physical and chemical properties. For example, strontium titanate ( $\text{SrTiO}_3$ , STO) has a centrosymmetric crystal lattice that prohibits the presence of polar functionalities, such as piezoelectricity, ferroelectricity, and pyroelectricity. However, Meirzadeh et al.<sup>[5]</sup> reported that the (100) surface of  $\text{TiO}_2$ -terminated STO is intrinsically pyroelectric at room temperature due to polar surface relaxation.

Surface reconstructions of STO have been previously reported.<sup>[99]</sup> For example, electron diffraction measurements show that the  $\text{TiO}_2$  terminated surface of STO undergoes surface relaxation whereby oxygen ions move outward from the surface relative to the titanium ions, which leads to a polarization of this layer.<sup>[100,101]</sup> Also, first-principles calculations show that SrO layers underneath the  $\text{TiO}_2$  display a polarization with an opposite sign, but lower in magnitude than that of the  $\text{TiO}_2$  surface layer.<sup>[102–104]</sup>

Meirzadeh et al.<sup>[5]</sup> show an intrinsic pyroelectric effect from a nanoscale region of  $\text{TiO}_2$ -terminated surface of STO (100) single crystal. This effect was detected using a setup that allows heating the surface of strontium titanate with fast infrared laser pulses and measuring how the resulting pyroelectric current evolves with time between the top and bottom electrodes (Figure 9a). The current was consistently generated between the electrodes over thousands of cycles without noticeable degradation. Since the local heating produced by the laser is very small, the strain

gradients induced by thermal expansion are insignificant and therefore neglected. The current rate decay follows the relationship  $I \propto 1/\sqrt{t}$  which is characteristic of a pyroelectric current dependence and implies that it originates from a thin polar layer near the surface of the crystal. Possible other external influences on the pyroelectric effect were also considered, that is, molecules absorbed to the surface, charges trapped by lattice defects, excitation of free electrons induced by light, and the thermoelectric Seebeck effect. The thickness of the polar layer was estimated to be  $\approx 1.2$  nanometers (3-unit cells). This observation is in good agreement with the result predicted by the first-principles calculations which show that polar distortion is formed at the surface of STO.<sup>[105]</sup> Although the magnitude of the pyroelectric coefficient differs slightly from sample to sample, the authors found that the surface polarity is a robust property for  $\text{TiO}_2$ -terminated STO single crystals. The polarization of the surface,  $P$ , was obtained by integrating  $\alpha\delta$  over the temperature range, where the thickness of the polar layer is constant (between 240 and 400 K (Figure 9b)). The polarization was found to be  $\approx 10 \mu\text{C cm}^{-2}$  at 280 K, a value which is comparable to the value of the strongly polar material  $\text{BaTiO}_3$  ( $25 \mu\text{C cm}^{-2}$ ).

Interestingly, the surface pyroelectricity of STO can be suppressed by introducing a few monolayers of  $\text{SiO}_2$ . This was verified experimentally and theoretically using DFT. Initially, the bulk of STO (100) single crystals have zero net charge. However, when the surface of STO is terminated with  $\text{TiO}_2$  the surface is relaxed by the distortion of the 3-unit cells closest to the surface to minimize the surface energy. When adding  $\text{SiO}_2$ , the polarization reverses sign relative to the uncapped STO surface, and the net polarization is cancelled (Figure 9c). Some surfaces seem to possess unique physical properties with respect to the bulk.<sup>[106–108]</sup> However, those reported surface layers tend to be much thicker than the one described in ref. [5] and are possibly induced by defects introduced during processing rather than being intrinsic polar.

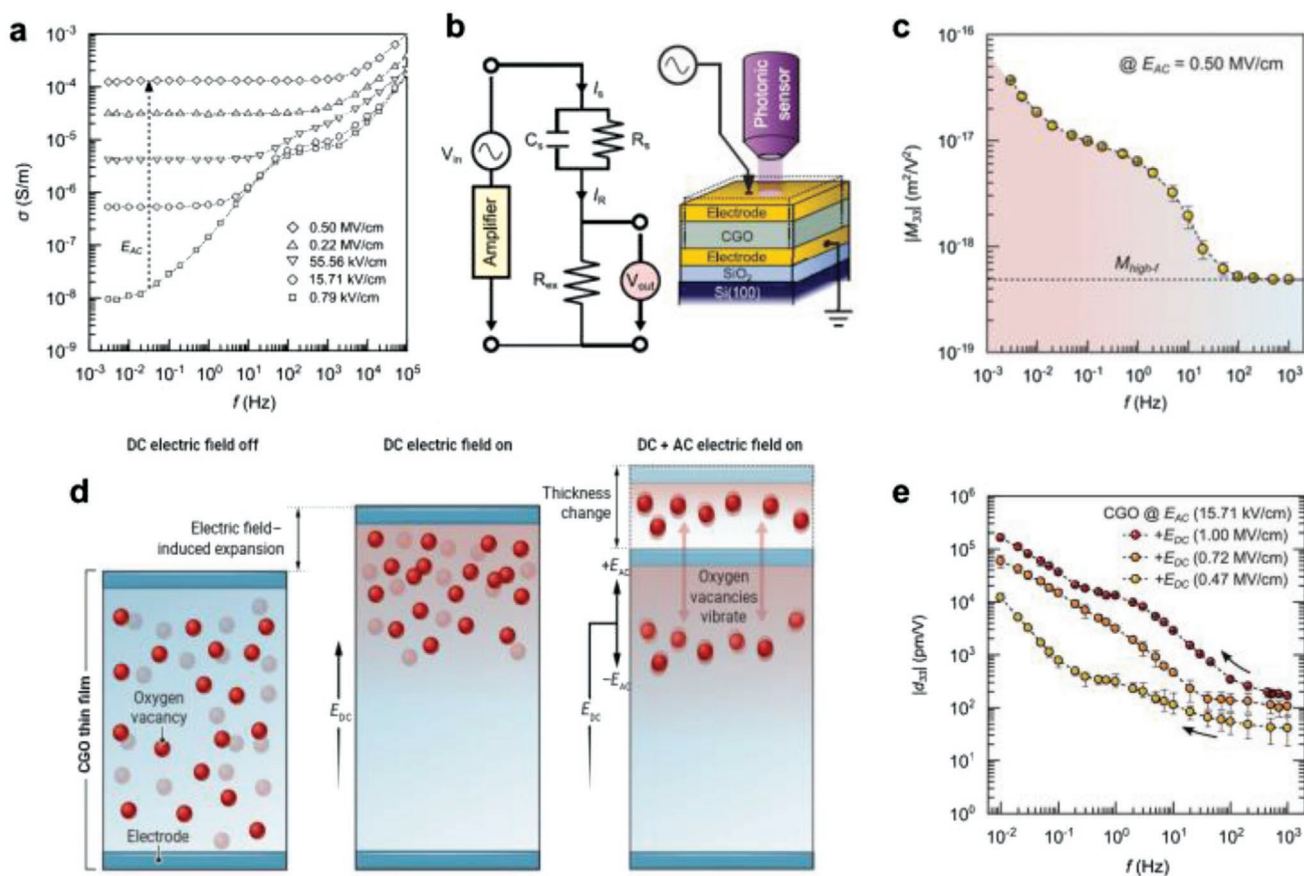


**Figure 8.** a) The frequency-dependent electrical conductivity of a CGO film sample as a function of applied  $E_{AC}$ .<sup>[3]</sup> The dc conductivity in the low-frequency regime ( $f < 1$  kHz) increases with increasing the  $E_{AC}$ . b) Schematic of the instrumental setup for the concurrent electrical and electromechanical displacement measurements for CGO capacitor samples. c) Electrostriction coefficients,  $|M_{33}|$ , of the CGO film as a function of measurement frequency, excited by  $E_{AC} = 0.5$  MV cm<sup>-1</sup>. d) Generation of the induced piezoelectric effects in a CGO film, which possesses mobile ionic defects ( $V_O$ ).<sup>[98]</sup> A macroscopic symmetry breaking of the CGO film can be driven by applying a static field ( $E_{DC}$ ), and the induced piezoelectric displacement can be generated via the control of an electric field, which is simultaneously composed of a large DC field and a small driving AC field. e) The apparent piezoelectric coefficients,  $|d_{33}|$ , of the CGO film as a function of  $f$ , excited by a constant driving AC field ( $E_{AC} = 15.71$  kV cm<sup>-1</sup>) and different DC fields ( $E_{DC} = +0.47$ ,  $+0.72$ , and  $+1.0$  MV cm<sup>-1</sup>).<sup>[3]</sup> Reproduced with permission.<sup>[3]</sup> Copyright 2022, The American Association for the Advancement of Science.

It is well known that all pyroelectric materials are also piezoelectric. Therefore, the observation of pyroelectricity at the STO surface also implies that it is intrinsically piezoelectric. Since STO is one of the most widely used substrates for thin films and multilayers, surface pyroelectricity and piezoelectricity would have substantial practical implications, such as tailoring polarization, pyroelectricity, and piezoelectricity by designing multilayered thin-film devices to take advantage of the surface polarization at the interface between each layer.<sup>[109,110]</sup> This finding opens the way for new applications in nanotechnology, electronics, and energy harvesting.

### 2.3.2. Interfaces in Ferroelectric Oxides

Apart from the effect of surfaces, piezoelectric and pyroelectric effects induced by symmetry breaking in otherwise centrosymmetric crystals can also happen at interfaces. Here, the interface in combination with external stimuli can break the inversion symmetry of centrosymmetric material. One possible

stimulus can be an electric field, playing a very similar role to the strain gradient in symmetry-breaking engineering.<sup>[111]</sup> The electric field can be either externally applied or a “built-in” potential, generally found at heterostructure interfaces and originating from band bending or a chemical potential gradient. This has already been used in 2D materials to engineer their non-centrosymmetry.<sup>[112–114]</sup>

Yang et al.<sup>[115]</sup> found that the built-in electric field originating from band bending at heterostructure interfaces could induce emergent piezoelectric and pyroelectric effects in centrosymmetric component materials. As schematically shown in **Figure 10a**, the electric field could induce symmetry breaking, where a crystal could only show the symmetry elements that are common to both the pristine crystal and the stimulus. Therefore, it’s possible to break the inversion symmetry of centrosymmetric materials and induces polar structures by an electric field. Figure 10b schematically shows the formation of the built-in electric field as a result of the band bending at the heterostructure interfaces, which points from the semiconductor to the noble metal. The coefficient of the induced piezoelectric effect is determined by

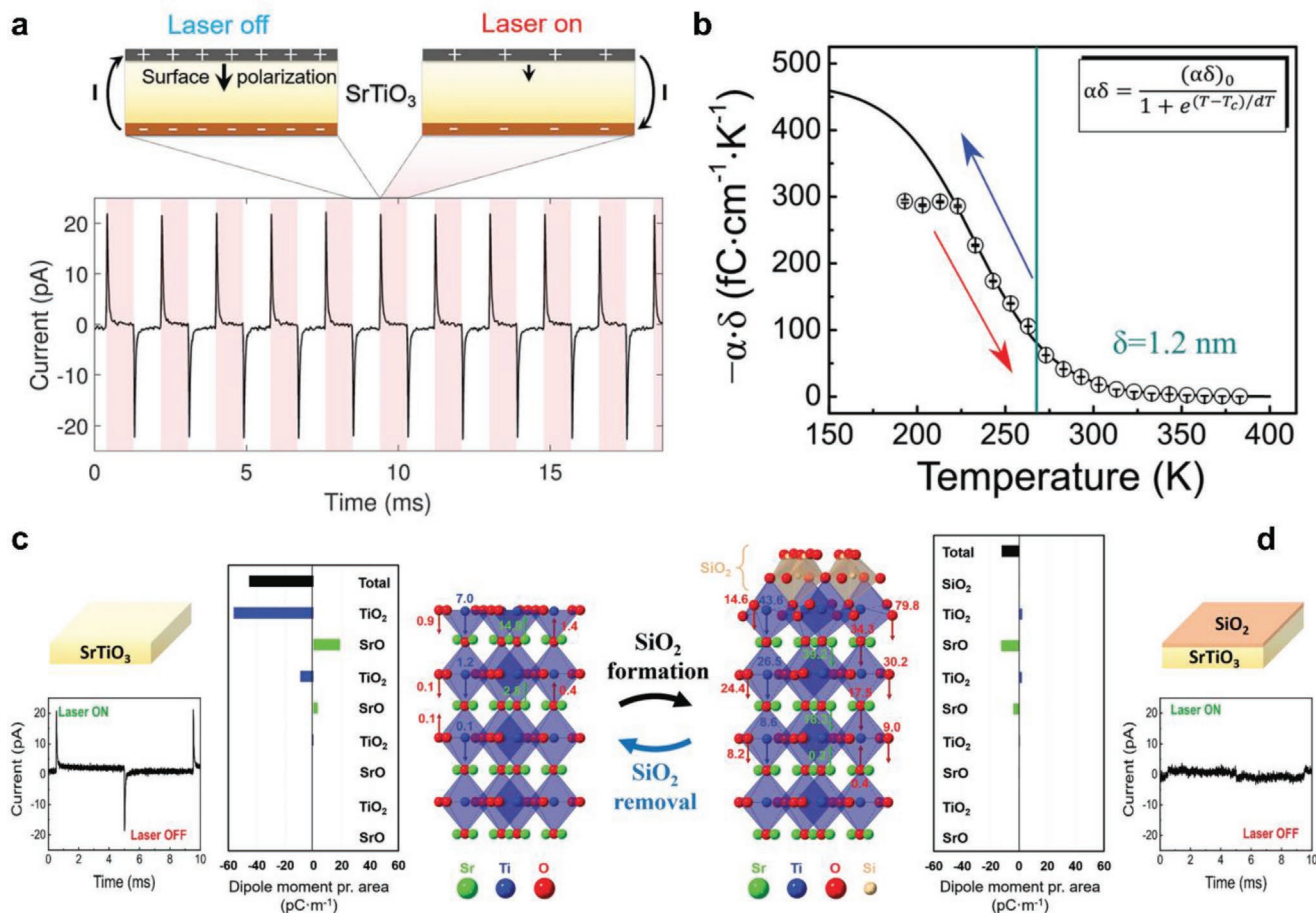


**Figure 9.** a) Change in the surface polarization and the pyroelectric current generated upon temperature change. b) Temperature dependence of the sheet pyroelectric coefficient ( $\alpha\delta$ ) and indication of a second-order phase transition. c) Turning surface pyroelectricity ON/OFF using SiO<sub>2</sub>.<sup>[5]</sup> Reproduced with permission.<sup>[5]</sup> Copyright 2019, Wiley-VCH.

$d_{ijk} = Q_{jki} \chi_3 \sqrt{2qN_d \chi_3 V_{bi}}$ , where  $d_{ijk}$ ,  $Q_{jki}$ ,  $\chi_3$ ,  $N_d$ , and  $V_{bi}$  are the induced piezoelectric coefficient, electrostriction coefficient, dielectric permittivity in the field direction, the effective donor density, and the built-in potential in the Schottky junction, respectively. Therefore,  $d_{ijk}$  is dependent on the physical properties of the semiconductor, especially the values of  $\chi_3$  and  $N_d$ . To demonstrate this effect, the authors have fabricated Schottky junctions by sputtering noble metal (Au) on (100)-orientated niobium (Nb)-doped SrTiO<sub>3</sub> (Nb:STO) and Nb-doped TiO<sub>2</sub> (Nb:TO) single crystals. The piezoelectric effect was observed and could be measured by applying dynamic stress to the crystal edges and collecting the short-circuit current generated by the junction. In addition, the Schottky junction also exhibits the pyroelectric effect, which originates from the temperature dependencies of the dielectric permittivity, the effective dopant density, and the built-in potential in the Schottky junctions.

The outcome of this work indicates that interface piezoelectricity and pyroelectricity could occur in heterostructures due to the existence of a built-in electric field at the interface. The interfacial effects could be induced in any heterostructures and thus are applicable to materials with any symmetry. Furthermore, the authors also demonstrated that the piezoelectric coefficients and pyroelectric coefficients can be substantially

improved, the magnitudes of which could be much higher than that of conventional bulk materials (Figures 10c and d).<sup>[115,116]</sup>

The design and fabrication of heterostructures have also been employed to create novel noncentrosymmetric states at the interface between the constituents,<sup>[117]</sup> which can lead to exotic electronic correlation phenomena.<sup>[109,115,118–120]</sup> To achieve this goal, precise atomic control of the interfaces as well as growth monitoring in real-time is required. In the study by Norlander et al.<sup>[121]</sup> inversion symmetry on a sub-unit-cell level was engineered in ultrathin hexagonal manganite films. By controlling the thickness (and therefore the interfaces) on the sub-unit-cell level, they managed to manipulate the material between a centrosymmetric and a noncentrosymmetric state. Deterministic control of inversion-symmetry breaking is needed in materials engineering, specifically to activate symmetry-controlled functionalities of epitaxially grown materials.

#### 2.4. Strain-Induced Electromechanics in Oxides

Integrating ferroelectrics onto nano- or micro-electromechanical devices has attracted substantial interest.<sup>[122,123]</sup> Strain engineering of thin films, that is, epitaxial strain, in this context



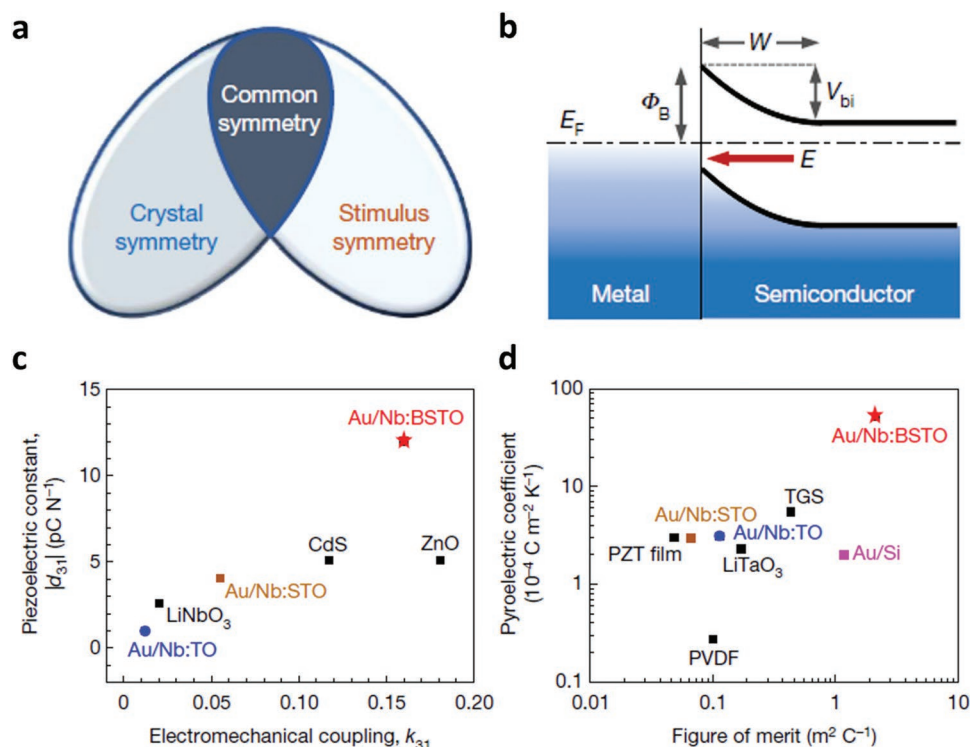


**Figure 10.** a) Schematic illustration of the engineering of crystal symmetry by external stimulus.<sup>[115]</sup> b) Schematic illustration of a Schottky junction, showing the potential variation in the depletion region. Note that  $E_F$ ,  $\Phi_B$ ,  $V_{bi}$ ,  $W$  and  $E$  represent the Fermi level, barrier height, built-in potential, depletion region, and electric field, respectively.<sup>[115]</sup> c) Comparison of piezoelectric constants ( $d_{31}$ ) and electromechanical coupling factors ( $k_{31}$ ).<sup>[115]</sup> d) Comparison of the pyroelectric coefficients and the figures of merit with other polar materials. Reproduced with permission.<sup>[115]</sup> Copyright 2020, The Author(s), under exclusive licence to Springer Nature Limited.

offers unique tunability for the physical properties and great opportunities for the fundamental understanding of ferroelectricity.<sup>[124,125]</sup> A coherent interface between materials can form if the lattice parameters of the film and the underlying substrate are close. When the lattice parameter of the substrate is larger/smaller than that of the thin film, the substrate will impart a tensile ( $\epsilon_{in-plane} > 0$ )/compressive ( $\epsilon_{in-plane} < 0$ ) strain onto the thin film by increasing/decreasing the atomic spaces along the in-plane direction of the film. Such strain breaks the inherent symmetry and has substantial effects in tuning the functionalities, such as inducing ferroelectricity in paraelectric, centrosymmetric crystals, improving ferroelectric polarization ( $P$ ), increasing the Curie temperature ( $T_C$ ), etc.<sup>[126–129]</sup>

In this section, we will first overview the effects of epitaxial strain on the structure evolution, such as the phase stability and domain morphology. We will then review the recent activities and new phenomena observed in freestanding oxide membranes. We will limit the discussion to ferroelectric, piezoelectric, and flexoelectric properties.

#### 2.4.1. Strain Induced Ferroelectricity in Centrosymmetric Oxides

At room temperature, strontium titanate ( $\text{SrTiO}_3$ , STO) is a perovskite centrosymmetric paraelectric. When cooled down, it remains paraelectric due to quantum fluctuations that prevent the formation of long-range ordering, even approaching its FE

transition temperature.<sup>[130,131]</sup> **Figure 11a** shows the phase diagram of STO as a function of strain and temperature. Strain is an effective approach to induce phase transition in STO and could lead to ferroelectricity even at room temperature. Under sufficiently large compressive strains, STO exhibits a tetragonal symmetry with polarization along the out-of-plane direction.<sup>[127]</sup> On the other hand, large in-plane tensile strains could rotate the polarization along the in-plane direction. Interestingly, the stability of the FE s increases with the increase of in-plane strain, irrespective of whether it is compressive or tensile. **Figure 11b** summarizes the maximum polarization ( $P_{max}$ ) and remnant polarization ( $P_r$ ) at different temperatures. The introduction of M/O-deficient (M for metal) perovskite nanoregions imposes a large in-plane tensile strain ( $\epsilon_{in-plane} = 3.8\%$ ) on the STO thin films, which exhibit rather high  $P_{max}$  and  $P_r$ , that is, 41.6 and 6.6  $\mu\text{C cm}^{-2}$ , respectively.<sup>[128]</sup> Such values are on the same order as that of  $\text{BaTiO}_3$  (26  $\mu\text{C cm}^{-2}$ ).<sup>[132]</sup> Moreover, the in-plane tensile strained tetragonal STO thin film exhibits a remarkably high Curie temperature ( $T_C$ ) up to 1098 K (**Figure 11c**) due to the “clamping” of the substrate, which is much higher than that of  $\text{BaTiO}_3$  (403 K) and  $\text{PbTiO}_3$  (763 K).<sup>[129,133]</sup>

Inducing ferroelectricity by strain was also observed in other centrosymmetric material systems. Based on density functional simulations (DFT), Bousequet et al.<sup>[134]</sup> show that ferroelectricity could be induced in simple binary oxides, that is, CaO, SrO, BaO, EuO, and their superlattice. Lee and Rabe<sup>[135]</sup> found that a strong spin-phonon coupling exists and results

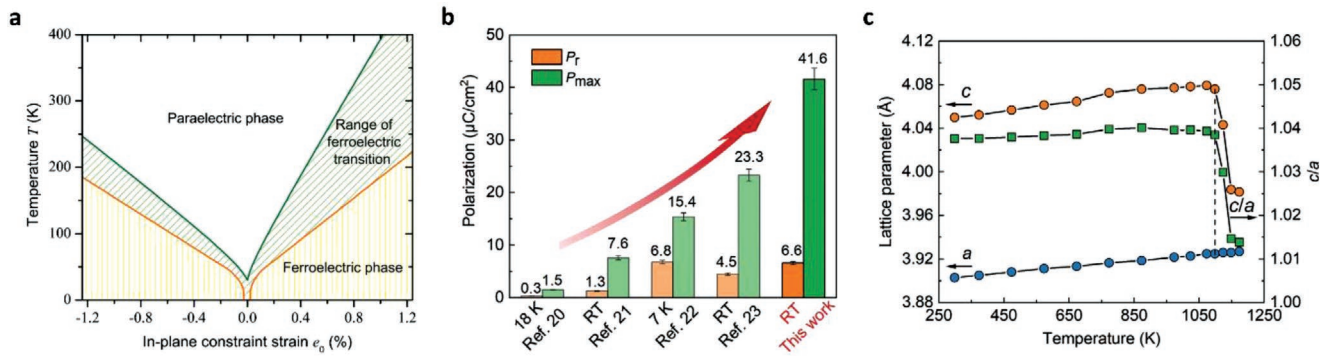


**Figure 11.** Strain-induced ferroelectricity in SrTiO<sub>3</sub> (STO). a) Phase diagram of STO as a function of strain and temperature without considering the antiferrodistortive distortions. Reproduced with permission.<sup>[127]</sup> Copyright 2006, American Physical Society. b) Comparisons of remnant polarization ( $P_r$ ) and maximum polarization ( $P_{max}$ ) obtained in different studies for STO thin films.<sup>[128]</sup> c) Temperature dependence of lattice parameters and  $c/a$  ratios for the thin film and substrate.<sup>[128]</sup> b,c) Reproduced with permission.<sup>[128]</sup> Copyright 2021, John Wiley and Sons.

in epitaxial strain-induced multiferroic phases in SrMnO<sub>3</sub>. By applying biaxial strain, the cubic bulk antiferromagnetic-paraelectric ground state could transform into a multiferroic state (e.g., both ferroelectric and ferromagnetic states), with a large spontaneous polarization (>50 μC cm<sup>-2</sup>) and a high magnetic Curie temperature ( $T_C > 92$  K). Another example is the epitaxial strain tuning of the phase stability of perovskite SrCoO<sub>3</sub>.<sup>[136]</sup> It has been found that both tensile and compressive strain could induce the phase transformation from the bulk ferromagnetic-metallic phase to antiferromagnetic-insulating FE. (Figure 12)

#### 2.4.2. Beyond Substrate: New Phenomena in Freestanding Membranes

Epitaxial growth has fundamental limitations: 1) discrete strain states due to limited single-crystalline substrates available; 2) limited combination of substrate and thin films with similar lattice parameters; 3) the strain-driven defect formation during high-temperature synthesis; 4) the reduction of relevant physical properties due to the clamping of the substrate. The recent development of freestanding oxide membranes circumvents such challenges.<sup>[138,139]</sup> Compared with bulk materials, freestanding membranes are much more robust to fracture and enable the application of large strains in a continuous way.<sup>[137,140,141]</sup>

Using Sr<sub>3</sub>Al<sub>2</sub>O<sub>6</sub> (SAO) as the sacrificial buffering layer, Xu et al.<sup>[137]</sup> have synthesized SrTiO<sub>3</sub> (STO) freestanding membranes (Figure 13a). By laminating the freestanding membranes onto a stretchable polymer substrate, the authors explored the strain-induced ferroelectricity and found that STO freestanding membranes exhibited robust room-temperature ferroelectricity under a uniaxial tensile strain (2%). This induced ferroelectricity is corroborated by the notable features of 180° ferroelectric domains with a Curie temperature up to 400 K (Figure 13b–h). The polymer substrates were stretched in the elastic deformation regime and enabled the creation of ferroelectricity and reversible control of the phase transition by strain, which provides the possibilities for designing various flexible ferroelectric devices. Using the same wet etching approach, Ji et al.<sup>[142]</sup> synthesized ultrathin perovskite films with high crystalline quality almost down to the monolayer limit and transferred them onto diverse

substrates. A systematic investigation by scanning transmission electron microscopy (STEM) demonstrated the high crystalline quality in the freestanding STO films with different thicknesses, including four-, three- and two-unit-cell-thick ones. Moreover, at a thickness of a few unit cells, the freestanding oxide films become flexible and can be bent and even folded back on themselves. This work demonstrates that there is no thickness limitation for stabilizing the crystalline order in freestanding ultrathin oxide films, thus offering new opportunities for research into 2D correlated phases and interfacial phenomena, with enormous potential for flexible multifunctional electronics applications.

While many oxides are extremely brittle in bulk, recent studies have shown that freestanding membranes are much more robust to fracture than their bulk counterparts. The mechanical properties are typically evaluated by Young's modulus ( $E$ ), which describes the mechanical loads required to elastically stretch and bend a material. By considering the contribution of the strain gradient  $\nabla\epsilon$  in addition to the strain ( $\epsilon$ ), the Gibbs free energy density ( $\phi$ ) can be expressed as

$$\phi = \frac{1}{2} E\epsilon^2 + \frac{1}{2} K(\nabla\epsilon)^2 \quad (2.1)$$

where  $K$  describes the energy coupling strength, and the second term is the strain gradient elasticity (SGE).

Flexoelectricity describes the generation of electric polarization ( $P$ ) induced by strain gradients ( $\nabla\epsilon$ ) that naturally break inversion symmetry, as schematically illustrated in Figure 13a. Since  $P = \mu\nabla\epsilon$ , and  $K = \mu^2/\chi$ , where  $\mu$  is the flexoelectric coefficient, Equation (2.1) could be converted to

$$\phi = \frac{1}{2} E\epsilon^2 + P^2/2\chi \quad (2.2)$$

Therefore, nanoscale flexoelectrics could make significant contributions to elasticity as  $P^2/2\chi$  becomes difficult to overcome when bending the crystal. Harbola et al.<sup>[143]</sup> have investigated the suspended STO crystalline membranes and found a nonmonotonic thickness dependence of Young's modulus upon small deflections, which corresponds to the linear (bending dominated,  $E_{lin}$ ) and cubic (stretching dominated,  $E_{cub}$ ) regions. This effect is demonstrated by the thickness dependence of the

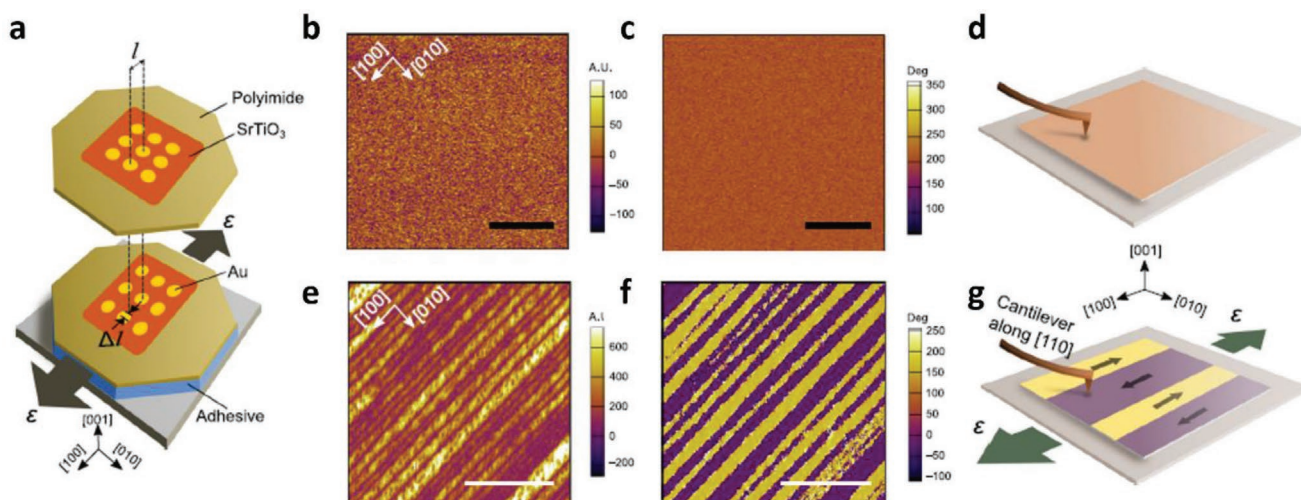


**Figure 12.** a) Schematic illustrating the stretching stage, wherein the strain is applied by fixing the STO membrane and polyimide sheet to a rigid substrate to maintain the strain state. The strain is calibrated using the ordered array of gold markers. b, c) Piezoresponse force microscopy amplitude and phase measured from unstrained membranes. The weak piezoresponse reveals the absence of room-temperature ferroelectricity, as illustrated in (d). e, f) Piezoresponse force microscopy amplitude and phase measured from 2.0% uniaxially strained (tensile) membranes. The notable 180° domain structures demonstrated the presence of room-temperature ferroelectricity, as illustrated in (g). Note that the scale bar is 1  $\mu\text{m}$ . Reproduced under the terms of a CC-BY license.<sup>[137]</sup> Copyright 2020, The Author(s), published by Springer Nature.

effective moduli:  $E_{\text{lin}}$  exhibits a minimum value of  $\approx 50$  GPa at  $t = 31$  nm, above which  $E_{\text{lin}}$  increases asymptotically toward the bulk value ( $\approx 300$  GPa). Below this thickness,  $E_{\text{lin}}$  increases sharply to  $\approx 250$  GPa at  $t = 14$  nm (Figure 13a,b). The nonmonotonicity and the presence of a minimum  $E_{\text{lin}}$  as a function of  $t$  are attributed to a crossover from a surface elasticity-dominated response to a strain gradient-dominated deformation response

as the thickness decreases. For  $t$  below 14 nm, the flexoelectric effect plays a dominant role in the elasticity ( $\text{SEG}, E_{\infty} + t^2$ ).<sup>[143]</sup> Furthermore, the same group found that STO membranes can withstand an elastic deformation with an average strain of  $\approx 6\%$  in the sub-20 nm thickness regime, which is more than an order of magnitude beyond the bulk limit. The membranes are highly resilient upon a high cycle fatigue test, surviving up

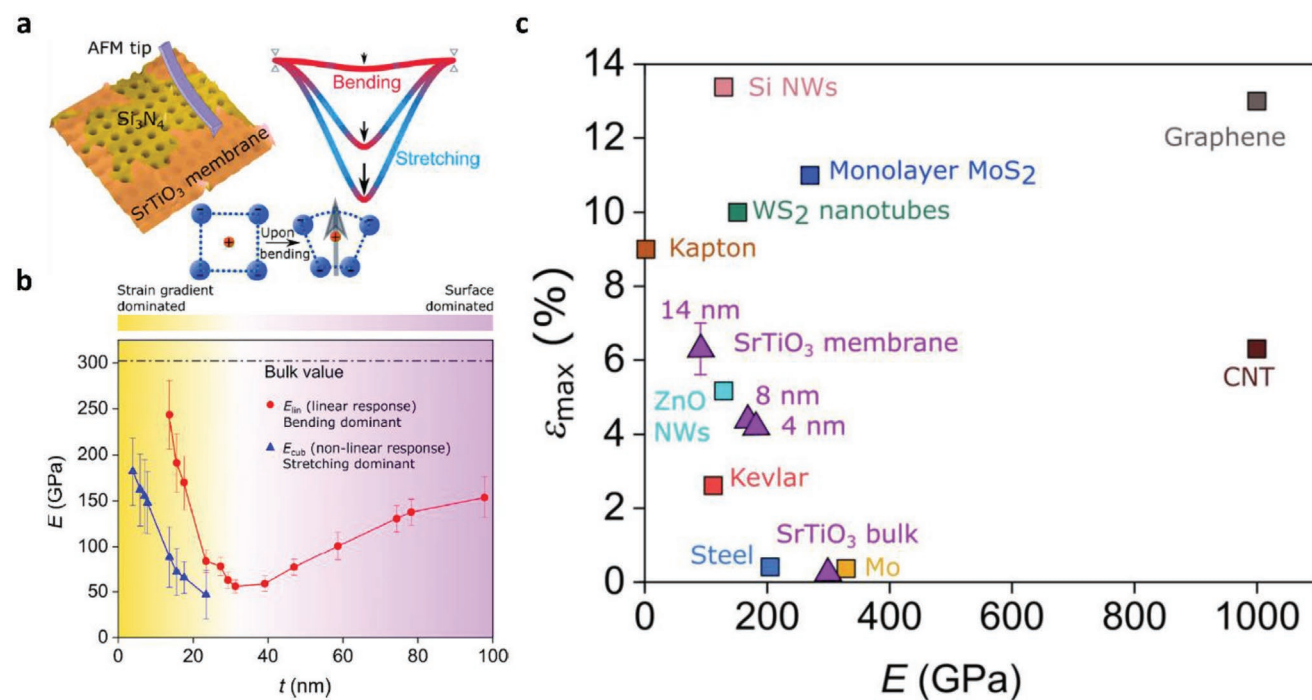


**Figure 13.** a) Schematic illustration of the characterization of the strain gradient elasticity in SrTiO<sub>3</sub> freestanding membranes. b) Thickness dependence of the effective Young's modulus of the SrTiO<sub>3</sub> membranes. a, b) Reproduced with permission.<sup>[143]</sup> Copyright 2021, American Chemical Society. c) The maximum tensile strain ( $\epsilon_{\text{max}}$ ) against the elastic modulus (E) for different materials. Reproduced with permission.<sup>[144]</sup> Copyright 2021, AIP Publishing.

to a billion cycles of force modulation at 85% of their fracture strain, demonstrating their high potential for nanomechanical applications.<sup>[144]</sup> Figure 13c summarizes the maximum tensile strain before fracture for various materials plotted against their elastic modulus. It is noted that the SrTiO<sub>3</sub> membranes compare extremely well with other nanomaterials, such as nanotubes and ZnO nanowires. It is also notable that these oxide membranes can bear up to about half the strain that graphene can withstand, which is the strongest material known thus far, and can sustain up to 13% strain before breaking.<sup>[144]</sup>

### 3. Perspective: Where Do We Go from Here?

Heterostructures of functional materials (and ferroelectrics in particular) have been a key point of interest for decades, both for fundamental research and for applications. However, the symmetry modulation at interfaces and the resultant outcomes have been largely overlooked. Here we have reported a variety of emergent electromechanical functionalities such as piezoelectricity and pyroelectricity where surfaces and interfaces induce symmetry-breaking effects into their centrosymmetric material components. However, to advance the field, some key fundamental and technological ingredients are still missing:

- 1) Better interfacial defect engineering of the heterostructures: a more detailed understanding is needed of the atomistic processes related to local inhomogeneities and chemistry.
- 2) Single-layer electroactive thin films will continue to be widely studied both from the fundamental science and applications points of view. Therefore, superlattices with a nanostructured asymmetric strain programmed into the lattice via the stacking order are still in their early stage and should be explored further.
- 3) Careful design of strain gradients and domain engineering is a way to improve material properties and achieve enhanced piezoelectric and pyroelectric coefficients.
- 4) Exploration of not only the practical applications of unconventional piezoelectric and ferroelectric phenomena, but also their integration into highly scaled next generation Si electronics remains key.
- 5) The inherent complexity of oxide materials requires the interrelation between the ab initio, atomistic modeling, and mesoscopic modeling tools. A robust cross-length scale modeling approach is therefore required.
- 6) Substantive spectroscopic evidence for defect types and densities at interfaces, which can provide unambiguous identification based on local structural information, is yet to be established.
- 7) For the foreseeable future, the dependence of material properties on the reduction of film thickness will remain a key hurdle toward obtaining more promising electromechanical materials.
- 8) The role of symmetries in the kinetics and dynamics of electromechanical materials is yet to be fully established.
- 9) Ferroelectric field control of material symmetry, which could yield new phenomena as a result of the strong coupling between chirality, spin, valley, etc.<sup>[145–147]</sup>

Research in the field of symmetry breaking in centrosymmetric materials is still in its infancy with regards to our fundamental understanding of the various mechanisms. Numerous interesting questions remain open and, no doubt, several new materials and structures are yet to be elaborated and discovered. We hope that our work will help researchers to understand the progress in electromechanical materials and encourage further investigations into this fascinating field.

### Acknowledgements

This research was supported by the BioWings project funded by the European Union's Horizon 2020, Future and Emerging Technologies (FET) programme (grant no. 801267). N.P. acknowledges the funding from the ERC Advanced "NEXUS" Grant 101054572. M.V. and V.E. acknowledge funding from Villum Fonden (Grant No 40412). This article is part of the Advanced Materials Interfaces Hall of Fame article series, which highlights the work of top interface and surface scientists.

### Conflict of Interest

The authors declare no conflict of interest.

### Keywords

chemical modification, electromechanical coupling, ferroelectricity, pyroelectricity, strain and strain gradient engineering, surface and interface engineering, symmetry breaking

Received: January 30, 2023

Revised: April 9, 2023

Published online: June 1, 2023

- [1] P. W. Anderson, *Science* **1972**, 177, 393.
- [2] V. Esposito, I. E. Castelli, *Adv. Mater. Interfaces* **2020**, 7, 1902090.
- [3] D. S. Park, M. Hadad, L. M. Riemer, R. Ignatans, D. Spirito, V. Esposito, V. Tileli, N. Gauquelin, D. Chezganov, D. Jannis, J. Verbeeck, S. Gorfman, N. Pryds, P. Mural, D. Damjanovic, *Science* **2022**, 375, 653.
- [4] H. Zhang, N. Pryds, D. S. Park, N. Gauquelin, S. Santucci, D. V. Christensen, D. Jannis, D. Chezganov, D. A. Rata, A. R. Insinga, I. E. Castelli, J. Verbeeck, I. Lubomirsky, P. Mural, D. Damjanovic, V. Esposito, *Nature* **2022**, 609, 695.
- [5] E. Meirzadeh, D. V. Christensen, E. Makagon, H. Cohen, I. Rosenhek-Goldian, E. H. Morales, A. Bhowmik, J. M. G. Lastra, A. M. Rappe, D. Ehre, M. Lahav, N. Pryds, I. Lubomirsky, *Adv. Mater.* **2019**, 31, 1904733.
- [6] C. Malgrange, C. Ricolleau, M. Schlenker, *Symmetry and Physical Properties of Crystals*, Springer, Dordrecht **2011**.
- [7] K. C. Kao, *Dielectric Phenomena in Solids: With Emphasis on Physical Concepts of Electronic Processes*, Elsevier, Amsterdam **2004**.
- [8] L. J. S. W. Kohn, *Phys. Rev.* **1965**, 140, A1133.
- [9] C. Chemistry, M. Modeling, *Computational Chemistry and Molecular Modeling*, Springer, Berlin, Heidelberg **2008**, pp. 297–310.
- [10] J. P. Perdew, K. Burke, M. Ernzerhof, *Phys. Rev. Lett.* **1996**, 77, 3865.
- [11] J. L. Lin, Y. Sun, R. He, Y. Li, Z. Zhong, P. Gao, X. Zhao, Z. Zhang, Z. J. Wang, *Nano Lett.* **2022**, 22, 7104.
- [12] Z. J. L. Bare, R. J. Morelock, C. B. Musgrave, *Adv. Funct. Mater.* **2022**, 32, 2200201.

- [13] G. A. Fiete, A. Rüegg, *J. Appl. Phys.* **2015**, *117*, 172602.
- [14] T. Xu, T. Shimada, Y. Araki, J. Wang, T. Kitamura, *Phys. Rev. B: Condens. Matter Mater. Phys.* **2015**, *92*, 104106.
- [15] J. Alaria, P. Borisov, M. S. Dyer, T. D. Manning, S. Lepadatu, M. G. Cain, E. D. Mishina, N. E. Sherstyuk, N. A. Ilyin, J. Hadermann, D. Lederman, J. B. Claridge, M. J. Rosseinsky, *Chem. Sci.* **2014**, *5*, 1599.
- [16] M.- Protocol, C. Cao, Y. Chen, Y. Wu, E. Deumens, *Int. J. Quantum Chem.* **2011**, *111*, 4020.
- [17] X. G. Zhao, Z. Wang, O. I. Malyi, A. Zunger, *Mater. Today* **2021**, *49*, 107.
- [18] A. P. Levanyuk, I. Burc Misirlioglu, M. Baris Okatan, *Ferroelectrics* **2020**, *569*, 310.
- [19] J. Zhu, H. Chen, X. Hou, L. Xu, H. Wu, J. Wang, *J. Appl. Phys.* **2019**, *125*, 234101.
- [20] C. Xie, H. Zhao, L. Du, H. Du, P. Wu, *Philos. Mag. Lett.* **2021**, *101*, 341.
- [21] L. Van Lich, T. Shimada, J. Wang, T. Kitamura, *Nanoscale* **2017**, *9*, 15525.
- [22] H. Simons, A. B. Haugen, A. C. Jakobsen, S. Schmidt, F. Stöhr, M. Majkut, C. Detlefs, J. E. Daniels, D. Damjanovic, H. F. Poulsen, *Nat. Mater.* **2018**, *17*, 814.
- [23] R. Maranganti, N. D. Sharma, P. Sharma, *Phys. Rev. B: Condens. Matter Mater. Phys.* **2006**, *74*, 014110.
- [24] E. Sahin, S. Dost, *Int. J. Eng. Sci.* **1988**, *26*, 1231.
- [25] Y. Lun, J. Hong, D. Fang, *J. Mech. Phys. Solids* **2022**, *164*, 104891.
- [26] W. Yang, X. Liang, S. Shen, *Acta Mech.* **2015**, *226*, 3097.
- [27] K. W. Böer, U. W. Pohl, *Semiconductor Physics* Springer Nature, Switzerland, AG **2022**.
- [28] Y. Sun, S. E. Thompson, T. Nishida, *Strain Effect in Semiconductors: Theory and Device Applications*, Springer, New York **2010**, pp. 1–350.
- [29] J. Bardeen, W. Shockley, *Phys. Rev.* **1950**, *80*, 72.
- [30] Y. Noguchi, H. Matsuo, Y. Kitanaka, M. Miyayama, *Sci. Rep.* **2019**, *9*, 4225.
- [31] Y. Kim, S. J. Kelly, A. Morozovska, E. K. Rahani, E. Strelcov, E. Eliseev, S. Jesse, M. D. Biegalski, N. Balke, N. Benedek, D. Strukov, J. Aarts, I. Hwang, S. Oh, J. S. Choi, T. Choi, B. H. Park, V. B. Shenoy, P. Maksymovych, S. V. Kalinin, *Nano Lett.* **2013**, *13*, 4068.
- [32] A. N. Morozovska, E. A. Eliseev, G. S. Svechnikov, S. V. Kalinin, *Phys. Rev. B: Condens. Matter Mater. Phys.* **2011**, *84*, 045312.
- [33] P. Sharma, S. Ryu, J. D. Burton, T. R. Paudel, C. W. Bark, Z. Huang, E. Y. T. Ariando, G. Catalan, C. B. Eom, A. Gruverman, *Nano Lett.* **2015**, *15*, 3547.
- [34] Y. Kim, A. N. Morozovska, A. Kumar, S. Jesse, E. A. Eliseev, F. Alibart, D. Strukov, S. V. Kalinin, *ACS Nano* **2012**, *6*, 7026.
- [35] A. Kholkin, I. Bdkin, T. Ostapchuk, J. Petzelt, *Appl. Phys. Lett.* **2008**, *93*, 222905.
- [36] B. Khanbabaee, E. Mehner, C. Richter, J. Hanzig, M. Zschornak, U. Pietsch, H. Stöcker, T. Leisegang, D. C. Meyer, S. Gorfman, *Appl. Phys. Lett.* **2016**, *109*, 222901.
- [37] N. Balke, S. Jesse, A. N. Morozovska, E. Eliseev, D. W. Chung, Y. Kim, L. Adamczyk, R. E. García, N. Dudley, S. V. Kalinin, *Nat. Nanotechnol.* **2010**, *5*, 749.
- [38] R. Schmitt, A. Nanning, O. Kraynis, R. Korobko, A. I. Frenkel, I. Lubomirsky, S. M. Haile, J. L. M. Rupp, *Chem. Soc. Rev.* **2020**, *49*, 554.
- [39] A. Kumar, F. Ciucci, A. N. Morozovska, S. V. Kalinin, S. Jesse, *Nat. Chem.* **2011**, *3*, 707.
- [40] Y. M. Kim, J. He, M. D. Biegalski, H. Ambaye, V. Lauter, H. M. Christen, S. T. Pantelides, S. J. Pennycook, S. V. Kalinin, A. Y. Borisevich, *Nat. Mater.* **2012**, *11*, 888.
- [41] S. V. Kalinin, N. A. Spaldin, *Science* **2013**, *341*, 858.
- [42] X. Chen, J. Yu, S. B. Adler, *Chem. Mater.* **2005**, *17*, 4537.
- [43] Y. Zhang-Steenwinkel, Q. Yu, F. P. F. Van Berkel, M. M. A. Van Tuel, B. Rietveld, H. Tu, *Int. J. Hydrogen Energy* **2016**, *41*, 5824.
- [44] S. Cheng, C. Chatzichristodoulou, M. Søgaard, A. Kaiser, P. V. Hendriksen, *J. Electrochem. Soc.* **2017**, *164*, F1354.
- [45] V. Esposito, E. Traversa, *J. Am. Ceram. Soc.* **2008**, *91*, 1037.
- [46] C. Sun, H. Li, L. Chen, *Energy Environ. Sci.* **2012**, *5*, 8475.
- [47] S. Schweiger, M. Kubicek, F. Messerschmitt, C. Murer, J. L. M. Rupp, *ACS Nano* **2014**, *8*, 5032.
- [48] T. Montini, M. Melchionna, M. Monai, P. Fornasiero, *Chem. Rev.* **2016**, *116*, 5987.
- [49] M. Pešić, F. P. G. Fengler, L. Larcher, A. Padovani, T. Schenk, E. D. Grimley, X. Sang, J. M. LeBeau, S. Slesazek, U. Schroeder, T. Mikolajick, *Adv. Funct. Mater.* **2016**, *26*, 4601.
- [50] P. Nukala, M. Ahmadi, Y. Wei, S. De Graaf, E. Stylianidis, T. Chakraborty, S. Matzen, H. W. Zandbergen, A. Björling, D. Mannix, D. Carbone, B. Kooi, B. Noheda, *Science* **2021**, *372*, 630.
- [51] S. Zafar, H. Jagannathan, L. F. Edge, D. Gupta, *Appl. Phys. Lett.* **2011**, *98*, 152903.
- [52] N. Yavo, A. D. Smith, O. Yehekel, S. Cohen, R. Korobko, E. Wachtel, P. R. Slater, I. Lubomirsky, *Adv. Funct. Mater.* **2016**, *26*, 1138.
- [53] R. Korobko, A. Patlolla, A. Kossoy, E. Wachtel, H. L. Tuller, A. I. Frenkel, I. Lubomirsky, *Adv. Mater.* **2012**, *24*, 5857.
- [54] R. E. Newnham, *Properties of Materials: Anisotropy, Symmetry, and Structure*, OUP, Oxford **2005**.
- [55] D. Damjanovic, *Rep. Prog. Phys.* **1998**, *61*, 1267.
- [56] F. Li, L. Jin, Z. Xu, S. Zhang, *Appl. Phys. Rev.* **2014**, *1*, 011103.
- [57] Q. M. Zhang, V. Bharti, X. Zhao, *Science* **1998**, *280*, 2101.
- [58] I. Urbanaviciute, X. Meng, M. Biler, Y. Wei, T. D. Cornelissen, S. Bhattacharjee, M. Linares, M. Kemerink, *Mater. Horiz.* **2019**, *6*, 1688.
- [59] R. E. Newnham, V. Sundar, R. Yimnirun, J. Su, Q. M. Zhang, *J. Phys. Chem. B* **1997**, *101*, 10141.
- [60] R. Korobko, A. Lerner, Y. Li, E. Wachtel, A. I. Frenkel, I. Lubomirsky, *Appl. Phys. Lett.* **2015**, *106*, 042904.
- [61] S. Santucci, H. Zhang, S. Sanna, N. Pryds, V. Esposito, *APL Mater.* **2019**, *7*, 071104.
- [62] E. Makagon, O. Kraynis, R. Merkle, J. Maier, I. Lubomirsky, *Adv. Funct. Mater.* **2021**, *31*, 2104188.
- [63] J. Yu, P. E. Janolin, *J. Appl. Phys.* **2022**, *131*, 170701.
- [64] D. P. Trujillo, A. Gurung, J. Yu, S. K. Nayak, S. P. Alpay, P. E. Janolin, *npj Comput. Mater.* **2022**, *8*, 251.
- [65] S. R. Bishop, D. Marrocchelli, C. Chatzichristodoulou, N. H. Perry, M. B. Mogensen, H. L. Tuller, E. D. Wachsman, *Annu. Rev. Mater. Res.* **2014**, *44*, 205.
- [66] D. Marrocchelli, S. R. Bishop, H. L. Tuller, B. Yildiz, *Adv. Funct. Mater.* **2012**, *22*, 1958.
- [67] R. Korobko, S. K. Kim, S. Kim, S. R. Cohen, E. Wachtel, I. Lubomirsky, *Adv. Funct. Mater.* **2013**, *23*, 6076.
- [68] N. Yavo, O. Yehekel, E. Wachtel, D. Ehre, A. I. Frenkel, I. Lubomirsky, *Acta Mater.* **2018**, *144*, 411.
- [69] M. Hadad, H. Ashraf, G. Mohanty, C. Sandu, P. Murali, *Acta Mater.* **2016**, *118*, 1.
- [70] S. Santucci, H. Zhang, S. Sanna, N. Pryds, V. Esposito, *J. Mater. Chem. A* **2020**, *8*, 14023.
- [71] H. Zhu, C. Yang, Q. Li, Y. Ren, J. C. Neuefeind, L. Gu, H. Liu, L. Fan, J. Chen, J. Deng, N. Wang, J. Hong, X. Xing, *Nat. Commun.* **2018**, *9*, 5063.
- [72] J. G. Swallow, J. J. Kim, J. M. Maloney, D. Chen, J. F. Smith, S. R. Bishop, H. L. Tuller, K. J. Van Vliet, *Nat. Mater.* **2017**, *16*, 749.
- [73] P. Gao, Z. Kang, W. Fu, W. Wang, X. Bai, E. Wang, *J. Am. Chem. Soc.* **2010**, *132*, 4197.
- [74] M. Varenik, J. C. Nino, E. Wachtel, S. Kim, S. R. Cohen, I. Lubomirsky, *ACS Appl. Mater. Interfaces* **2021**, *13*, 20269.
- [75] M. Varenik, J. C. Nino, E. Wachtel, S. Kim, O. Yehekel, N. Yavo, I. Lubomirsky, *ACS Appl. Mater. Interfaces* **2020**, *12*, 39381.
- [76] A. Kabir, S. Santucci, N. Van Nong, M. Varenik, I. Lubomirsky, R. Nigon, P. Murali, V. Esposito, *Acta Mater.* **2019**, *174*, 53.
- [77] T. Defferriere, D. Kalaev, J. L. M. Rupp, H. L. Tuller, *Adv. Funct. Mater.* **2021**, *31*, 2005640.

- [78] B. Malic, T. Rojac, *Nat. Mater.* **2018**, *17*, 297.
- [79] W. Peng, J. Mun, Q. Xie, J. Chen, L. Wang, M. Kim, T. W. Noh, *npj Quantum Mater.* **2021**, *6*, 48.
- [80] J. Maier, *Phys. Chem. Chem. Phys.* **2009**, *11*, 3011.
- [81] A. Bencan, G. Drazic, H. Ursic, M. Makarovic, M. Komelj, T. Rojac, *Nat. Commun.* **2020**, *11*, 1762.
- [82] F. A. Kröger, H. J. Vink, *Solid State Phys.* **1956**, *3*, 307.
- [83] A. Kabir, J. R. Bowen, M. Varenik, I. Lubomirsky, V. Esposito, *Materialia* **2020**, *12*, 100728.
- [84] A. Kabir, V. Buratto Tinti, M. Varenik, I. Lubomirsky, V. Esposito, *Mater. Adv.* **2020**, *1*, 2717.
- [85] H. Zhang, I. E. Castelli, S. Santucci, S. Sanna, N. Pryds, V. Esposito, *Phys. Chem. Chem. Phys.* **2020**, *22*, 21900.
- [86] A. Kabir, H. Zhang, S. Colding-Jørgensen, S. Santucci, S. Molin, V. Esposito, *Scr. Mater.* **2020**, *187*, 183.
- [87] M. Yan, T. Mori, J. Zou, J. Drennan, *J. Am. Ceram. Soc.* **2009**, *92*, 2745.
- [88] C. Artini, *Inorg. Chem.* **2018**, *57*, 13047.
- [89] V. B. Tinti, A. Kabir, J. K. Han, S. Molin, V. Esposito, *Nanoscale* **2021**, *13*, 7583.
- [90] R. Ramesh, D. G. Schlom, *Nat. Rev. Mater.* **2019**, *4*, 257.
- [91] J. Jiang, L. Zhang, C. Ming, H. Zhou, P. Bose, Y. Guo, Y. Hu, B. Wang, Z. Chen, R. Jia, S. Pendse, Y. Xiang, Y. Xia, Z. Lu, X. Wen, Y. Cai, C. Sun, G. C. Wang, T. M. Lu, D. Gall, Y. Y. Sun, N. Koratkar, E. Fochtung, Y. Shi, J. Shi, *Nature* **2022**, *607*, 480.
- [92] X. Xi, L. Zhao, Z. Wang, H. Berger, L. Forró, J. Shan, K. F. Mak, *Nat. Nanotechnol.* **2015**, *10*, 765.
- [93] and J. F. M. Kubicek, Z. Cai, W. Ma, B. Yildiz, H. Hutter, *ACS Nano* **2013**, *7*, 3276.
- [94] W. S. Choi, J. H. Kwon, H. Jeon, J. E. Hamann-Borrero, A. Radi, S. MacKe, R. Sutarto, F. He, G. A. Sawatzky, V. Hinkov, M. Kim, H. N. Lee, *Nano Lett.* **2012**, *12*, 4966.
- [95] N. Pryds, V. Esposito, *J. Electroceram.* **2017**, *38*, 1.
- [96] S. E. Park, T. R. Shrout, *J. Appl. Phys.* **1997**, *82*, 1804.
- [97] D. A. Egger, *Nature* **2022**, *609*, 680.
- [98] F. Li, *Science* **2022**, *375*, 618.
- [99] G. Z. Zhu, G. Radtke, G. A. Botton, *Nature* **2012**, *490*, 384.
- [100] N. Bickel, G. Schmidt, K. Heinz, K. Müller, *Phys. Rev. Lett.* **1989**, *62*, 2009.
- [101] N. Erdman, K. R. Poeppelmeier, M. Asta, O. Warschkow, D. E. Ellis, L. D. Marks, *Nature* **2002**, *419*, 55.
- [102] E. Heifets, E. A. Kotomin, J. Maier, *Surf. Sci.* **2000**, *462*, 19.
- [103] E. Heifets, R. I. Eglitis, E. A. Kotomin, J. Maier, G. Borstel, *Surf. Sci.* **2002**, *513*, 211.
- [104] S. Kim, O. Sinai, C. W. Lee, A. M. Rappe, *Phys. Rev. B: Condens. Matter Mater. Phys.* **2015**, *92*, 235431.
- [105] E. Bishenden, D. J. Donaldson, *J. Phys. Chem. A* **1998**, *102*, 4638.
- [106] P. M. Gehring, K. Hirota, C. F. Majkrzak, G. Shirane, *Phys. Rev. Lett.* **1993**, *71*, 1087.
- [107] N. Domingo, N. Bagués, J. Santiso, G. Catalan, *Phys. Rev. B: Condens. Matter Mater. Phys.* **2015**, *91*, 094111.
- [108] K. Hirota, J. P. Hill, S. M. Shapiro, G. Shirane, Y. Fujii, *Phys. Rev. B* **1995**, *52*, 13195.
- [109] N. Sai, B. Meyer, D. Vanderbilt, *Phys. Rev. Lett.* **2000**, *84*, 5636.
- [110] H. Yamada, M. Kawasaki, Y. Ogawa, Y. Tokura, *Appl. Phys. Lett.* **2003**, *81*, 4793.
- [111] S. W. Cheong, *npj Quantum Mater.* **2019**, *4*, 53.
- [112] S. J. Papadakis, E. P. De Poortere, H. C. Manoharan, M. Shayegan, R. Winkler, *Science* **1999**, *283*, 2056.
- [113] S. Wu, J. S. Ross, G. Bin Liu, G. Aivazian, A. Jones, Z. Fei, W. Zhu, D. Xiao, W. Yao, D. Cobden, X. Xu, *Nat. Phys.* **2013**, *9*, 149.
- [114] H. Yuan, X. Wang, B. Lian, H. Zhang, X. Fang, B. Shen, G. Xu, Y. Xu, S. C. Zhang, H. Y. Hwang, Y. Cui, *Nat. Nanotechnol.* **2014**, *9*, 851.
- [115] M. M. Yang, Z. D. Luo, Z. Mi, J. Zhao, S. P. E. M. Alexe, *Nature* **2020**, *584*, 377.
- [116] R. W. Whatmore, *Rep. Prog. Phys.* **1986**, *49*, 1335.
- [117] H. Y. Hwang, Y. Iwasa, M. Kawasaki, B. Keimer, N. Nagaosa, Y. Tokura, *Nat. Mater.* **2012**, *11*, 103.
- [118] A. Ohtomo, H. Y. Hwang, *Nature* **2004**, *427*, 423.
- [119] C. Song, S. Havlin, H. A. Makse, *Nature* **2005**, *433*, 392.
- [120] C. Becher, M. Trassin, M. Lilienblum, C. T. Nelson, S. J. Suresha, D. Yi, P. Yu, R. Ramesh, M. Fiebig, D. Meier, *Nat. Commun.* **2014**, *5*, 4295.
- [121] J. Nordlander, M. D. Rossell, M. Campanini, M. Fiebig, M. Trassin, *Nano Lett.* **2021**, *21*, 2780.
- [122] R. A. McKee, F. J. Walker, M. F. Chisholm, *Science* **2001**, *293*, 468.
- [123] S. H. Baek, J. Park, D. M. Kim, V. A. Aksyuk, R. R. Das, S. D. Bu, D. A. Felker, J. Lettieri, V. Vaithyanathan, S. S. N. Bharadwaja, N. Bassiri-Gharb, Y. B. Chen, H. P. Sun, C. M. Folkman, H. W. Jang, D. J. Kreft, S. K. Streiffer, R. Ramesh, X. Q. Pan, S. Trolier-McKinstry, D. G. Schlom, M. S. Rzhowski, R. H. Blick, C. B. Eom, *Science* **2011**, *334*, 958.
- [124] D. G. Schlom, L. Q. Chen, C. B. Eom, K. M. Rabe, S. K. Streiffer, J. M. Triscone, *Annu. Rev. Mater. Res.* **2007**, *37*, 589.
- [125] H. Wang, F. Tang, P. H. Dhuwad, X. Wu, *npj Comput. Mater.* **2020**, *6*, 52.
- [126] J. H. Haeni, P. Irvin, W. Chang, R. Uecker, P. Reiche, Y. L. Li, S. Choudhury, W. Tian, M. E. Hawley, B. Craigo, A. K. Tagantsev, X. Q. Pan, S. K. Streiffer, L. Q. Chen, S. W. Kirchoefer, J. Levy, D. G. Schlom, *Nature* **2004**, *430*, 758.
- [127] Y. L. Li, S. Choudhury, J. H. Haeni, M. D. Biegalski, A. Vasudevarao, A. Sharan, H. Z. Ma, J. Levy, V. Gopalan, S. Trolier-McKinstry, D. G. Schlom, Q. X. Jia, L. Q. Chen, *Phys. Rev. B: Condens. Matter Mater. Phys.* **2006**, *73*, 184112.
- [128] T. Li, S. Deng, H. Liu, S. Sun, H. Li, S. Hu, S. Liu, X. Xing, J. Chen, *Adv. Mater.* **2021**, *33*, 2008316.
- [129] K. J. Choi, M. Biegalski, Y. L. Li, A. Sharan, J. Schubert, R. Uecker, P. Reiche, Y. B. Chen, X. Q. Pan, V. Gopalan, L. Q. Che, D. C. Schlom, C. B. Eom, *Science* **2004**, *306*, 1005.
- [130] K. A. Müller, H. Burkard, *Phys. Rev. B* **1979**, *19*, 3593.
- [131] K. A. Müller, W. Berlinger, E. Tosatti, *Properties of Perovskites and Other Oxides*, Vol. 277583, World Scientific Publishing Co. Pte. Ltd, Singapore **2010**, p. 495.
- [132] B. Jaffe, W. R. Cook, H. Jaffe, *Piezoelectric Ceramics*, Academic, London, UK **1971**, p. 77.
- [133] L. Zhang, J. Chen, L. Fan, O. Diéguez, J. Cao, Z. Pan, Y. Wang, J. Wang, M. Kim, S. Deng, J. Wang, H. Wang, J. Deng, R. Yu, J. F. Scott, X. Xing, *Science* **2018**, *361*, 494.
- [134] E. Bousquet, N. A. Spaldin, P. Ghosez, *Phys. Rev. Lett.* **2010**, *104*, 037601.
- [135] J. H. Lee, K. M. Rabe, *Phys. Rev. Lett.* **2010**, *104*, 2.
- [136] J. H. Lee, K. M. Rabe, *Phys. Rev. Lett.* **2011**, *107*, 067601.
- [137] R. Xu, J. Huang, E. S. Barnard, S. S. Hong, P. Singh, E. K. Wong, T. Jansen, V. Harbola, J. Xiao, B. Y. Wang, S. Crossley, D. Lu, S. Liu, H. Y. Hwang, *Nat. Commun.* **2020**, *11*, 3141.
- [138] F. M. Chiabrera, S. Yun, Y. Li, R. T. Dahm, H. Zhang, C. K. R. Kirchert, D. V. Christensen, F. Trier, T. S. Jespersen, N. Pryds, *Ann. Phys.* **2022**, *534*, 2200084.
- [139] D. Pesquera, A. Fernández, E. Khestanova, L. W. Martin, *J. Phys.: Condens. Matter* **2022**, *34*, 383001.
- [140] D. Lu, D. J. Baek, S. S. Hong, L. F. Kourkoutis, Y. Hikita, H. Y. Hwang, *Nat. Mater.* **2016**, *15*, 1255.
- [141] L. Han, Y. Fang, Y. Zhao, Y. Zang, Z. Gu, Y. Nie, X. Pan, *Adv. Mater. Interfaces* **2020**, *7*, 1901604.
- [142] D. Ji, S. Cai, T. R. Paudel, H. Sun, C. Zhang, L. Han, Y. Wei, Y. Zang, M. Gu, Y. Zhang, W. Gao, H. Huan, W. Guo, D. Wu, Z. Gu, E. Y. Tsybal, P. Wang, *Nature* **2019**, *570*, 87.
- [143] V. Harbola, S. Crossley, S. S. Hong, D. Lu, Y. A. Birkh, Y. Hikita, H. Y. Hwang, *Nano Lett.* **2021**, *21*, 2470.
- [144] H. Y. H. Varun Harbola, R. Xu, S. Crossley, P. Singh, *Appl. Phys. Lett.* **2021**, *119*, 053102.

- [145] Q. Wang, Y. Gu, C. Chen, F. Pan, C. Song, *J. Phys. Chem. Lett.* **2022**, *13*, 10065.
- [146] L. Zhang, J. Jiang, C. Multunas, C. Ming, Z. Chen, Y. Hu, Z. Lu, S. Pendse, R. Jia, M. Chandra, Y. Y. Sun, T. M. Lu, Y. Ping, R. Sundararaman, J. Shi, *Nat. Photonics* **2022**, *16*, 529.
- [147] Y. Hu, F. Florio, Z. Chen, W. A. Phelan, M. A. Siegler, Z. Zhou, Y. Guo, R. Hawks, J. Jiang, J. Feng, L. Zhang, B. Wang, Y. Wang, D. Gall, E. F. Palermo, Z. Lu, X. Sun, T. M. Lu, H. Zhou, Y. Ren, E. Wertz, R. Sundararaman, J. Shi, *Sci. Adv.* **2020**, *6*, eaay4213.



**Haiwu Zhang** is a postdoctoral researcher at the Technical University of Denmark, Department of Energy Conversion and Storage. His research focuses on the design and engineering of complex oxide thin films, heterostructures, and freestanding membranes for the development of advanced functional materials, such as ferroelectrics/piezoelectrics, electrostrictors, fast ionic conductors.



**Nini Pryds** is a professor and head of the research section "Functional Oxide" at the Department of Energy Conversion and Storage, The Technical University of Denmark (DTU), where he is leading a group of researchers working in the field of complex oxide thin films for applications in a wide range of energy and information technologies. He made major contributions in emerging disciplines such as Nanoionics and Iontronics, dealing with the design and control of interface-related phenomena in fast ionic and electronic conductors. His main interest is aimed at exploring how broken symmetries at interfaces affect magnetic, electronic, and ionic properties.